

Dynamic Forcing Behind Hurricane Lidia's Rapid Intensification

Mauricio López-Reyes^{1,2,3}, María Luisa Martín^{4,5}, Carlos Calvo-Sancho^{4,6}, Juan Jesús González-Alemán⁷

¹Instituto de Astronomía y Meteorología (IAM), Centro Universitario de Ciencias Exactas e Ingenierías (CUCEI), Departamento de Física, Universidad de Guadalajara, Guadalajara, Mexico.

²Department of Earth Physics and Astrophysics, Faculty of Physics, Complutense University of Madrid, Madrid, Spain.

³Instituto Frontera A.C., Departamento de Investigación, Tijuana, México.

⁴Department of Applied Mathematics, Faculty of Computer Engineering, University of Valladolid, Spain.

⁵Institute of Interdisciplinary Mathematics (IMI), Complutense University of Madrid, Madrid, Spain.

⁶Centro de Investigaciones sobre Desertificación, Consejo Superior de Investigaciones Científicas (CIDE, CSIC-UV-Generalitat Valenciana), Climate, Atmosphere and Ocean Laboratory (Climatoc-Lab), Moncada, Valencia, Spain

⁷Department of Development and Applications, Agencia Estatal de Meteorología (AEMET), Madrid, Spain.

Corresponding author: C. Calvo-Sancho (carlos.calvo.sancho@uva.es)

Key words

Rapid intensification, ensemble prediction, tropical cyclone, extratropical interactions

Key points

- A mid-to-upper level trough enhanced vertical motion and divergence over Hurricane Lidia, triggering rapid intensification.
- Stronger Trenberth forcing, eddy flux convergence, and vorticity advection were observed in ensemble members that captured RI.
- Ensemble diagnostics revealed that dynamic forcing preceded RI onset, suggesting a causal role beyond thermodynamic conditions.

Abstract

This study examines Hurricane Lidia's rapid intensification (RI) in the understudied northeastern Pacific, focusing on its interaction with an upper-level trough. Using IFS-ECMWF ensemble forecasts and ERA5 reanalysis, we analyze the large-scale dynamical mechanisms driving Lidia's intensification. Results show that the trough played a crucial role in promoting RI by enhancing synoptic-scale ascent, upper-level divergence, and eddy flux

43 convergence. In the higher-intensification ensemble group, a coherent sequence emerged
44 in which enhanced negative Trenberth forcing appeared several hours before RI onset,
45 followed by marked increases in upper-level divergence, cyclonic vorticity advection, and
46 mid-tropospheric moistening. These signals collectively reduced vertical wind shear over the
47 storm and strengthened the upper-level outflow, creating an environment highly conducive
48 to RI. In contrast, the lower-intensification group exhibited weaker forcing, higher shear, and
49 a lack of sustained divergence in upper levels. These findings highlight the importance of
50 diagnosing early dynamical triggers for RI, particularly in regions where operational access
51 to high-resolution models is limited. A conceptual schematic synthesizes these multi-stage
52 processes, highlighting how upper-level dynamical forcing and favorable thermodynamic
53 conditions acted jointly to precondition and then accelerate RI. This approach provides a
54 cost-effective framework for anticipating RI using ensemble-based diagnostics and could
55 serve as a valuable forecasting tool in data-sparse areas such as the Pacific coast of Mexico.
56 Future studies should combine this large-scale methodology with high-resolution
57 simulations to better capture storm-scale processes and validate multi-scale interactions in
58 RI events.

59
60
61
62
63
64
65
66
67
68
69
70
71
72
73
74
75
76
77
78
79
80
81
82
83
84
85
86

1 Introduction

México is among the countries most affected by tropical cyclones (TCs) from both the Atlantic and Pacific Oceans (Larson et al., 2005; López-Reyes et al., 2024). While the Atlantic basin has traditionally garnered more research attention, largely due to the severe economic and social impacts of TCs in the United States, there is a pressing need to expand research efforts in the northeastern Pacific basin, where fewer studies have been conducted (García Franco et al., 2024). In recent years, various major hurricanes, such as Patricia, Lidia, and Otis caused large economic losses and scores of deaths in México (Pasch, 2024; García Franco et al., 2024). These events also posed challenges for numerical weather prediction models, particularly in forecasting their tracks and intensification processes. As highlighted by Shi and Chen (2021), one of the key obstacles is improving the prediction of TCs that undergo rapid intensification (RI), defined as an increase of at least 30 kt (≈ 54 km/h) in maximum sustained wind speed within a 24-h period (Kaplan and DeMaria, 2003). Recent studies have shown a rise in the frequency of RI events in the Atlantic basin, driven primarily by ocean warming (Majumdar et al., 2023; Li et al., 2023). The northeastern Pacific, however, has also experienced extreme intensification rates, with Patricia (2015), Willa (2018), and Otis (2023) ranking among the most rapidly intensifying storms on record. Similarly, during the 2024 hurricane season, Hurricane Milton underwent explosive intensification, posing a significant challenge for intensity forecasting (Pasch, 2024). Enhancing our ability to forecast RI is essential for reducing the risk these powerful storms pose to vulnerable communities and critical infrastructure.

Although RI is strongly influenced by thermodynamic factors, such as high sea surface temperatures (SSTs) and ocean heat content, dynamic factors also play a pivotal role. Interactions between TCs and upper-level troughs have been shown to significantly affect storm intensity (Fischer et al., 2019). According to Avila (1998), Hanley et al. (2001), López-Reyes et al. (2021) and DeMaria et al. (2021), forecasting intensity changes in TCs remains one of the biggest challenges, particularly during RI. The difficulties in forecasting RI stem from the complex factors involved in the occurrence of RI, such as the large-scale environment, internal dynamics and multiscale interactions (Kaplan et al., 2010; Zhang and Chen 2012; Bhalachandran et al., 2020; Wang et al., 2021; Shi and Chen 2021). Over the past few years, there has been notable progress in understanding the internal dynamics that govern RI. As found in Chen et al. (2019) and Shi and Chen, key internal dynamical and thermodynamic features associated with RI include strong upper-level divergence and strong boundary-layer convergence as well as a weak deep-layer vertical wind shear (VWS), higher relative humidity throughout the vertical column, and high intensification potential (details in Emanuel, 1988) associated with SST. Other studies have highlighted the significance of the deep convective region surrounding the eyewall and the large convergence of angular momentum into TC (Stevenson et al., 2014; Komaromi and Doyle 2018; Ryglicki et al., 2021).

While these internal mechanisms are primary to the intensification process, the surrounding environment can modulate RI by providing dynamically favorable conditions,

131 such as upper-level forcing or favorable trough interactions. From a kinematic perspective,
132 however, changes in intensity ultimately result from the TC's ability to evacuate mass from
133 the boundary layer through convection and draw in angular momentum, as recently
134 emphasized by Montgomery and Smith (2025) and Smith et al. (2021). Furthermore,
135 research studies have identified a relevant relationship between the structure and size of
136 TCs, their environmental conditions, and the **TC intensification rate** (Carrasco et al., 2014;
137 Shi and Chen 2019; Tao et al., 2022; Ston et al., 2023; Nayaranan et al., 2024).

138

139 Since the general conditions favoring TC RI are well-known, other factors may influence
140 the overall intensification processes. In a follow-up theoretical study, Leroux et al. (2016)
141 identified an optimal TC-trough alignment that promotes interaction (Komaromi and Doyle
142 2018; Shato et al., 2020). Similarly, studies by DeMaria et al. (1993), Hanley et al. (2001),
143 and Peirano et al. (2016) suggest that an approaching upper-tropospheric trough can play a
144 critical role in hurricane intensification. However, trough interactions can also limit TC
145 intensification, depending on the configuration of the trough and its associated jet stream.
146 For example, increased dry air entrainment or increased VWS can inhibit TC development
147 (Peirano et al., 2016). Recent research has identified specific synoptic configurations that
148 favor RI, including short zonal wavelengths and favorable upstream displacements between
149 the TC and the trough (Fischer et al., 2019). Qiu et al. (2020) also showed how important
150 eddy flux convergence (EFC) is for identifying trough interactions, particularly when large-
151 scale circulation patterns favor stronger upper-level divergence. In the same way, Yan et al.
152 (2021) found that upper-tropospheric cold lows could enhance EFC, reduce inertial stability,
153 and strengthen upper-level divergence, leading to RI. These studies show that TC-trough
154 interactions can have two effects and stress how important it is to figure out what
155 environmental conditions make TCs stronger or weaker.

156

157 Although TC–trough interactions have been extensively studied in the Atlantic basin, the
158 northeastern Pacific remains understudied. During El Niño events, the subtropical Pacific
159 warms considerably, increasing the likelihood of interactions between TCs and the jet
160 stream, increasing the likelihood of dynamic interactions (Luna-Niño et al., 2021; Ling et al.,
161 2024). On the other hand, these interactions often occur at higher latitudes over less
162 populated areas in the Atlantic basin. In contrast, TCs in the northeastern Pacific tend to
163 curve toward land, which puts densely populated areas in Mexico at risk. The fact that warm
164 SSTs and the jet stream interact during El Niño events shows how important it is to do
165 focused research in this area.

166

167 The most intense hurricanes that have affected Mexico typically occur during late
168 summer and early autumn, as was the case with Hurricane Lidia in mid-October 2023. The
169 devastating case of Hurricane Otis in October 2023, in which all global models failed to
170 capture its RI, underscored the urgent need for improved understanding of RI processes in
171 this region. Hurricane Lidia underwent an unusual RI just off the Pacific coast of Mexico in
172 October 2023, surprising forecasters and resulting in widespread damage. Despite the
173 proximity to land and under moderate VWS, the storm rapidly intensified and made landfall
174 as a Category 4 hurricane (Pasch, 2024). The failure of operational models to predict this

175 intensification (as in the case of Hurricane Otis the same month) underscores the urgent
176 need to improve the understanding the dynamical processes involved in such cases.
177 Additionally, the proximity of northeastern Pacific TCs to mountainous terrain introduces
178 further challenges for forecasting (DiMego et al., 1976). This event caused dozens of
179 fatalities and severe and widespread damages in Acapulco, highlighting Mexico's
180 vulnerability to such phenomena and the critical need for better forecast capabilities
181 (Servicio Meteorológico Nacional, 2023; Emanuel, 2024). Given the high SSTs during this
182 season, trough-TC interaction is particularly relevant during October and November, as
183 many TCs turn eastward during this period. This turning is influenced by the subtropical jet
184 stream, typically positioned between 25°N and 35°N, especially during seasons when El Niño
185 events are present (Luna-Niño et al., 2021; Tong et al., 2023). The jet stream may enhance
186 interactions between midlatitude troughs TCs.

187
188 While the underlying dynamics of these interactions may be broadly similar across
189 ocean basins, the eastern North Pacific exhibits unique characteristics that justify a
190 focused investigation. In particular, the variability of the subtropical jet, often
191 modulated by ENSO (Liu et al., 2024), differs from typical Atlantic configurations (Zhao
192 and Raga, 2015; Winters and Attard, 2022), and the recurving behavior of TCs toward the
193 Mexican coastline during late-season months creates a distinct synoptic context. To
194 the authors' knowledge, no previous studies have specifically investigated the role of the jet
195 stream in TC RI in the northeastern Pacific. In contrast to most prior studies in the Atlantic
196 basin, which primarily focus on thermodynamic drivers, our research emphasizes the
197 dynamical forcing mechanisms relevant to the eastern North Pacific, particularly those
198 associated with trough–TC interactions, such as quasi-geostrophic (QG) ascent, EFC, and
199 enhanced upper-level divergence in the intensification of Hurricane Lidia. By analyzing
200 ensemble prediction system (EPS) outputs and ERA5 reanalysis data, we provide a
201 comprehensive assessment of the conditions that favored Lidia's RI, offering novel insights
202 into the dynamics of TC intensification in the northeastern Pacific.

203
204 While operational mesoscale models such as the Hurricane Analysis and Forecast System
205 (HAFS) now provide high-resolution forecasts for TCs in the eastern North Pacific, ensemble
206 prediction systems (EPS) like those from the European Centre for Medium-Range Weather
207 Forecasts (ECMWF) offer publicly accessible data and have demonstrated strong skill in
208 capturing the uncertainty associated with complex and potentially high-impact TC scenarios.
209 Therefore, ensemble-based diagnostics remain a valuable and scalable approach for
210 assessing TC behavior and RI risks, particularly in resource-constrained forecasting
211 environments such as Mexico.

212
213 This paper is organized as follows: Section 2 presents the data models and methods,
214 including the ensemble configurations and diagnostics tools. Section 3 describes the
215 synoptic conditions that influenced Hurricane Lidia's RI and discusses the main dynamical
216 processes involved; a conceptual schematic summarizing these processes is also presented.
217 Finally, Section 4 provides a summary of findings and concluding remarks.

218

219 **2 Data Models and Methods**

220

221 The data sets are based on forecasts from the Integrated Forecasting System (IFS) of the
 222 ECMWF. This study uses the operational perturbed forecast ensemble generated by the EPS
 223 (Cycle 48r1: ECMWF, 2023) with 50 perturbed members is used. Each perturbed member
 224 has a horizontal resolution of 0.1° and 137 vertical levels. The last initialization is selected
 225 since it features a large spread of Hurricane Lidia trajectories, corresponding to the October
 226 8th, 00:00 UTC initialization, which spans a 96-hour forecast window with 1 h time steps.
 227 Additionally, to assess the performance of each composite group, key atmospheric fields are
 228 computed using data from the ERA5 climate reanalysis (Hersbach et al., 2020) with 0.25°
 229 horizontal resolution and 37 vertical levels, during the period with the highest intensification
 230 rate.

231

232 Several dynamic and thermodynamic variables were utilized in this study, such as mean
 233 sea level pressure (*MSLP*), temperature (*T*), geopotential height (*Z*), zonal and meridional
 234 wind components (*u, v*), potential temperature (θ), SST and relative humidity (*RH*). See
 235 Table 1 for additional details. To evaluate the role of the trough in the trajectory and
 236 intensity change of Hurricane Lidia we analyzed trajectories and intensification rate for all
 237 members using MSLP and grouped into two intensification rate groups (IRGs) based on the
 238 P_{20} (lower intensification rate) and P_{80} (highest intensification rate) percentiles of MSLP.
 239 These percentiles were calculated using the minimum central pressure attained by each
 240 ensemble member during the 24 h period of most rapid intensification (October 9, 00:00
 241 UTC to October 10, 00:00 UTC) and were cross-validated using the maximum sustained wind
 242 speed to ensure that they met the official RI definition (greater than 54
 243 $km\ h^{-1}$ in 24 h). The NHC best track and official intensity data were used for comparison
 244 with both groups. As is common in studies of this nature (Chen et al., 2019; Chen et al.,
 245 2021; Hu and Zou, 2021; Collins et al., 2022), synoptic and storm-centered composites (SCC)
 246 are derived for the specified fields within a circular area with an 8° radius.

247 **Table 1.** Details on the atmospheric variables used.

Variable	Symbol	Pressure levels (PVU)	Units
Mean sea level pressure	<i>MSLP</i>	Surface	<i>hPa</i>
Temperature	<i>T</i>	Surface, 1000, 925, 850, 700, 500, 400, 300, 250, 200	<i>K</i>
Geopotential height	<i>Z</i>	1000, 925, 850, 700, 500, 400, 300, 250, 200	<i>m</i>
Zonal wind component	<i>u</i>	850, 300, 200	ms^{-1}
Meridional wind component	<i>v</i>	850, 300, 200	ms^{-1}
Potential temperature	θ	(1.5-PVU)	<i>K</i>
Sea surface temperature	<i>SST</i>	Surface	<i>K</i>
Relative humidity	<i>RH</i>	500 hPa	%

248

249 Based on the previous variables, some derived fields related with TC intensity change
 250 (Chen et al., 2021; Mei and Yu 2016) are also computed: VWS calculated between 850 and

251 200 hPa , between 0-500 km radius, irrotational wind (\vec{V}_{irr}) at 200 hPa, based on Helmholtz
 252 decomposition (details in Chorin et al., 1990 and Cao et al., 2014) and vorticity advection,
 253 $\vec{V} \cdot \nabla(\vec{\xi} + f)$ at 500 hPa, where $\vec{\xi} = \frac{\partial v}{\partial x} - \frac{\partial u}{\partial y}$ and f is the planetary vorticity.

254

255 Following Bister and Emanuel (1998) and Gilford (2021), potential intensity (PI) is also
 256 calculated as

257

$$258 \quad PI = V_{max} = \left[\frac{C_k (T_s - T_0)}{C_D T_0} (h_s^* - h^*) \right]^{1/2},$$

259

260 where C_k is the enthalpy surface exchange coefficient, C_D is the momentum surface
 261 exchange coefficient, h_s^* is the saturation moist static energy at the sea surface, h^* is the
 262 saturation moist static energy of the air above the boundary layer, following to Wing et al.
 263 (2015), evaluated at 500-600 hPa. As mentioned in Gilford (2021), tropical cyclone
 264 thermodynamic disequilibrium and efficiency were represented by terms $(h_0^* - h^*)$ and
 265 $\frac{T_s - T_0}{T_0}$, where T_s is the sea surface temperature and T_0 is the outflow temperature level.

266

267 To identify regions that favor ascending air movements driven by synoptic-scale
 268 dynamical forcing associated with extratropical systems (Loughe et al., 1995; Hanley et al.,
 269 2001), ageostrophic wind (\vec{V}_{ag}) and its divergence ($\nabla \cdot \vec{V}_{ag}$) are additionally computed. The
 270 QG omega equation is also used to identify the synoptic ascent flow via Trenberth form
 271 (Billingsley, 1998; Bracken and Bosart, 2000). Trenberth QG forcing (Q) is calculated using
 272 the following expression

273

$$274 \quad Q = \left(\sigma \nabla_p^2 + f_0^2 \frac{\partial^2}{\partial p^2} \right) \omega \approx 2 \left[f_0 \frac{\partial \vec{V}_g}{\partial p} \cdot \nabla \left(\frac{\partial v}{\partial x} - \frac{\partial u}{\partial y} + f \right) \right], \quad (1)$$

275

276 i.e., vertical air movements are proportional to advection by vorticity by thermal wind.
 277 Herein, σ is the stability parameter, f_0 the Coriolis parameter, ω the vertical component of
 278 wind ($Pa \cdot s^{-1}$), \vec{V}_g the geostrophic wind vector ($m s^{-1}$), p the pressure (Pa). To minimize
 279 the influence of small-scale noise and mesoscale features in the diagnostic fields, a spatial
 280 Gaussian filter ($\sigma = 1.5^\circ$) was first applied uniformly to the entire domain, preserving the
 281 synoptic-scale variability. In addition, to reduce potential contamination from the TC's own
 282 circulation, an additional localized Gaussian filtering was applied to the Q dynamical forcing
 283 fields within an 800 km radius centered on the storm, with a smooth cosine taper toward
 284 the surrounding environment. This procedure effectively attenuates the contribution of the
 285 TC's inner-core vorticity while maintaining the continuity and coherence of the synoptic-
 286 scale trough and jet stream features.

287

288 Finally, with the aim of measuring the degree of interaction between the trough and
 289 the TC, and following previous studies in the Atlantic Ocean (Molinari and Vollaro, 1990;
 290 Hanley et al., 2000; Komaromi and Doyle, 2018), the eddy flux convergence (EFC) is defined
 291 as

292 $EFC = -\frac{1}{r^2} \frac{\partial}{\partial r} (r^2 \overline{v'_r v'_t}),$ (2)
293

294 where v'_r is the perturbation radial wind, v'_t the perturbation tangential wind, and the
295 overbar denotes the azimuthal mean, computed in storm-relative coordinates. Based on the
296 methodology of DeMaria et al. (1993) and Hanley et al. (2001), the EFC is computed over a
297 radial range of 300 to 600 km for each time step during RI period. The calculation spans the
298 full 96 h forecast period starting from the model initialization, thereby encompassing pre-
299 RI, RI, and post-RI phases for both ERA5 and members groups.

300 To compare atmospheric fields between the most and least intensifying groups,
301 averages and standard deviations (STD) are calculated, and ensemble difference spatial
302 distributions ($P_{80} - P_{20}$) are generated to visualize the contrasts between the two groups.
303 In addition, time series of means and STDs of the thermodynamic and dynamic variables
304 analyzed between the groups during the simulation period are performed. Finally, a Mann-
305 Whitney U test is performed to identify regions with statistically significant differences at
306 the 95% confidence level (Mann and Whitney, 1947).

307

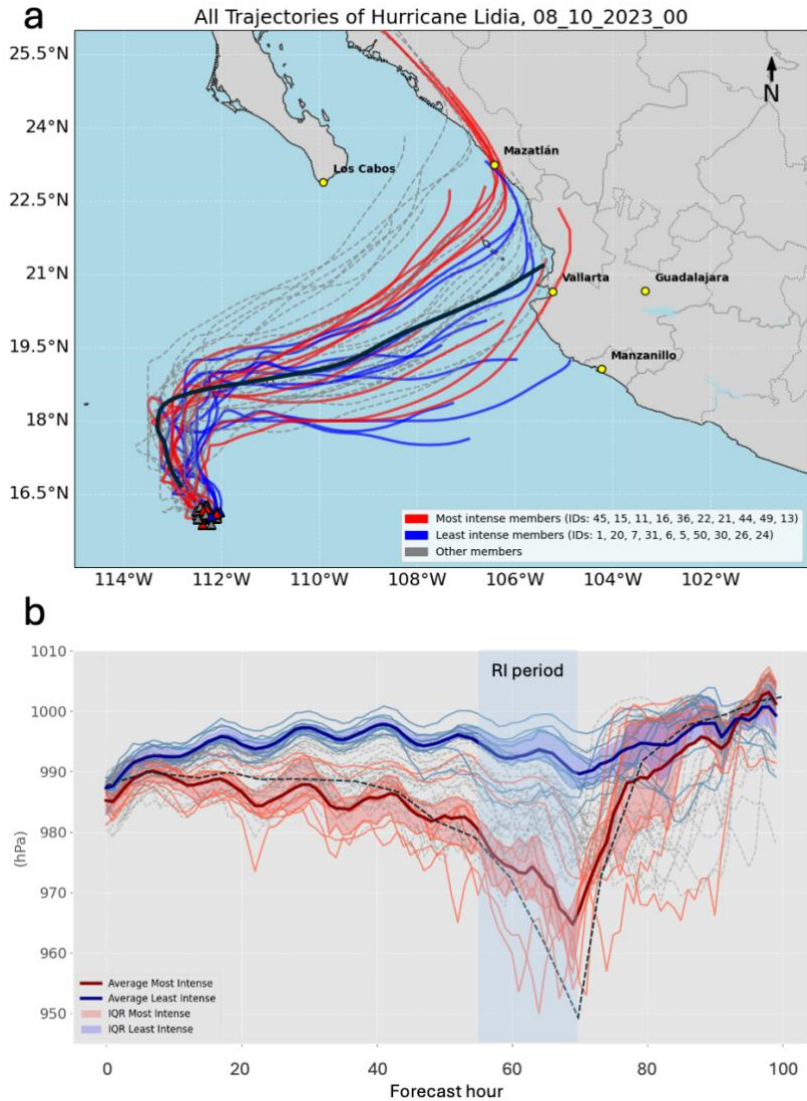
308 **3 Results**

309

310 **3.1 Trajectory and intensity forecast analysis.**

311 Hurricane Lidia originated from a tropical wave on 3 October 2023 (Pasch, 2024).
312 Between 3 and 5 October, it remained a disorganized system, marked by significant
313 uncertainty in both track and intensity forecasts (Figures S1). From 5 to 7 October, Lidia
314 generally tracked westward under the influence of a mid-level ridge but remained poorly
315 organized. By 8 October, the subtropical jet stream was positioned between 20° and 30°N,
316 aligned with Lidia's latitude (Figures A1 and 2 in Appendix). At this stage, a mid-to-upper-
317 level trough approaching the Baja California Peninsula began to influence Lidia's motion,
318 steering the system northward and subsequently eastward.

319 At approximately 18:00 UTC on 9 October, Lidia entered a phase of intensification
320 (Pasch, 2024). This intensification was accompanied by a northeastward turn induced by an
321 approaching trough from the northwest, although considerable spread in forecast
322 trajectories persisted at this time (Fig. 1a). On 10 October, Lidia underwent RI, with
323 maximum sustained winds increasing by 82 km h^{-1} over an 18-hour period, ultimately
324 reaching a peak intensity of nearly 220 km h^{-1} . This placed Lidia at Category 4 on the Saffir-
325 Simpson Hurricane Wind Scale.



326

327

Figure 1. (a) Lidia’s Trajectories for all members, highest (lower) IRG in red (blue) line and best track of NHC (black line). (b) Intensity temporal evolution for all members (MSLP), highest (lower) IRG in red (blue) line, shaded areas correspond with interquartile range; official MSLP in black dotted line.

331

332

Figure 1a shows the trajectories of Hurricane Lidia’s ensemble members from the ECMWF, initialized at 00:00 UTC on 8 October. The trajectories of the most intense members are positioned further north relative to those of the lower-intensity members, relative to the NHC best track. This suggests that the trough’s proximity influenced event predictability, increasing uncertainty in both track and intensity forecasts (Figures A1 and 2 in Appendix). This pattern aligns with findings from Ito and Wu (2013), Callaghan (2020), and Sato et al. (2020) in the Atlantic basin, indicating the contribution of synoptic environment to the low predictability of both trajectory and intensity of the cyclone, as here evidenced by the large spread in Figures 1a, b. Furthermore, based on the temporal evolution of Lidia’s MSLP and

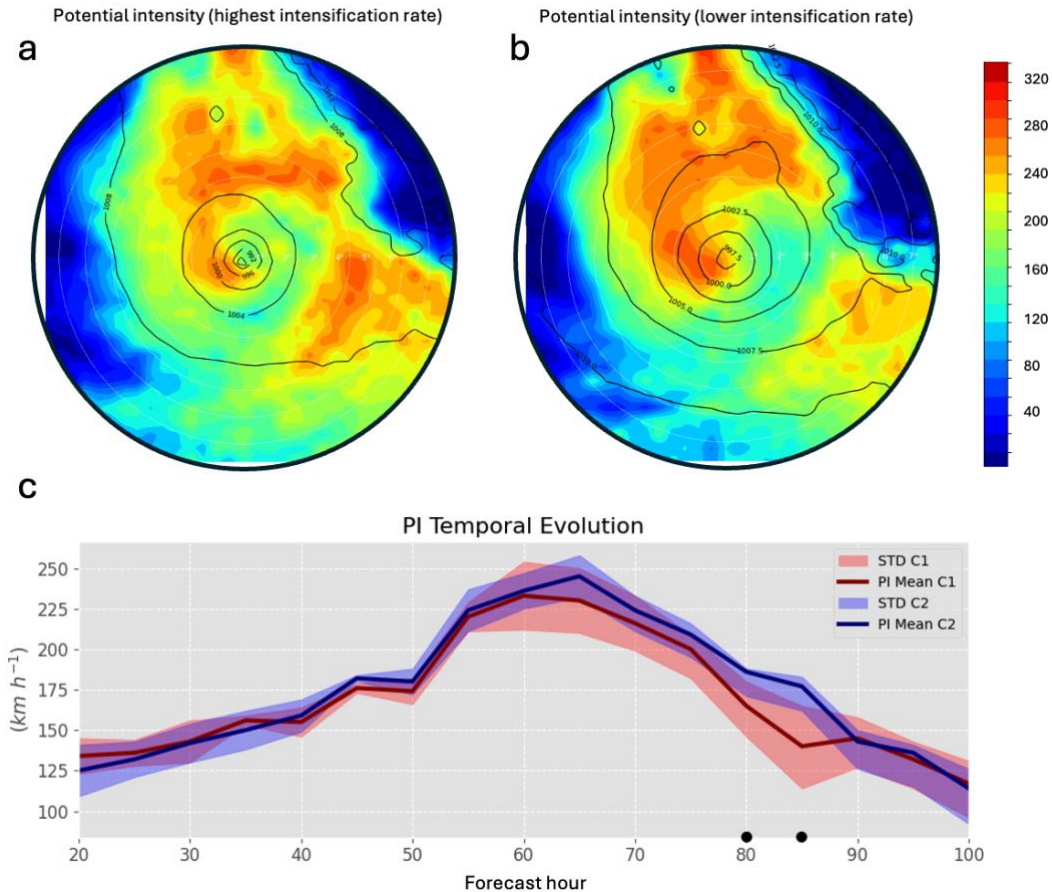
340

341 wind speed (Fig. 1b), seven members in the P_{80} -ensemble group, along with the ensemble
342 mean, successfully simulate Lidia's rapid intensification, exceeding the RI threshold.
343

344 As is well known and formulated in the Emanuel model (Emanuel, 2002) and used in
345 Chen et al. (2021), the oceanic and atmospheric variables such as T_s , T_0 and saturation
346 parameters (eq. 1), determine the PI that the TC could acquire. Both ensembles display
347 similar PI distributions around Hurricane Lidia (Figs. 2a, b). However, somewhat
348 unexpectedly the P_{20} -ensemble shows a higher PI value ($\sim 250 \text{ km h}^{-1}$) compared to the
349 P_{80} -ensemble ($\sim 240 \text{ km h}^{-1}$), although the differences are not statistically significant (not
350 shown).
351

352 Based on the PI time series (Fig. 2c), this diagnostic variable alone does not appear to
353 support Lidia's RI. Therefore, this suggests that thermodynamic factors are necessary but
354 not sufficient to trigger RI. This finding is consistent with recent studies (e.g., Gilford, 2021;
355 Shi and Chen, 2021) which suggest that while PI provides an upper bound, the actual
356 intensification process is modulated by environmental dynamics, including ventilation and
357 vertical motion induced by synoptic-scale features such as upper-level troughs. These results
358 highlight the potential value of ensemble forecasts for anticipating RI events under favorable
359 environmental and synoptic conditions. In the following sections, we examine the temporal
360 evolution and structural characteristics of the large-scale dynamical forcing, including the
361 trough interaction, to support this interpretation.

362 Similarity, the spatial SST differences between the P_{80} - and P_{20} -ensembles (Fig. 3a–f)
363 reinforce the conclusion that thermodynamic conditions alone do not explain the
364 contrasting intensification outcomes. While some localized differences exceeding $\pm 5^\circ\text{C}$
365 appear at specific time steps, these do not persist or align consistently with the RI period.
366 The warm anomalies observed in the P_{20} -ensemble are mainly displaced to the north and
367 northeast of Lidia's core. This spatial misalignment suggests that, despite slightly warmer
368 SSTs, the coupling between oceanic energy supply and inner-core dynamics was likely
369 suboptimal.

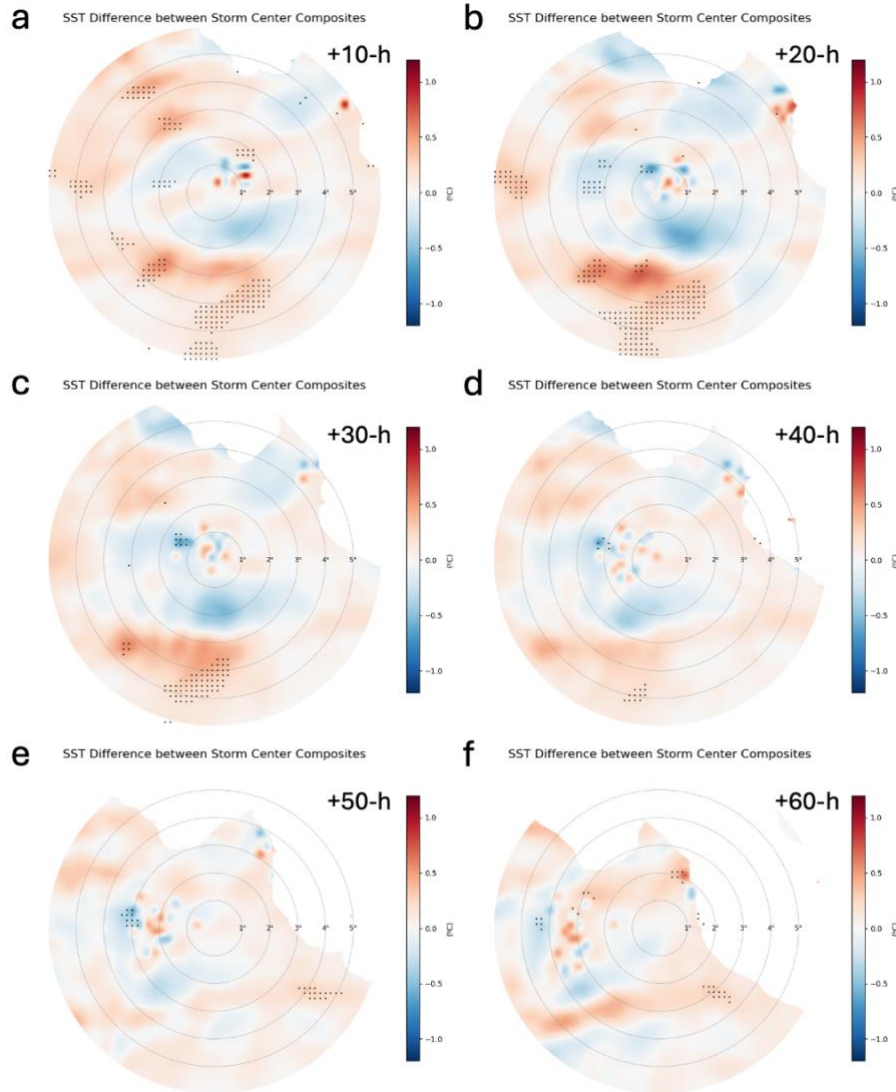


370 Figure 2. (a) Highest intensification rate PI SCC and (b) lower intensification rate PI SCC
 371 ($km\ h^{-1}$) at +55-h and (c) PI computed within a radial range of 6° , with the red (blue)
 372 line representing the higher (lower) IRG. The red (blue) shaded regions indicate the STD for the
 373 highest (lower) IRG.
 374

375 Statistical significance markers confirm that most SST anomalies are not spatially
 376 coherent enough to produce systematic differences in PI. This is consistent with the similar
 377 PI fields seen in both ensembles (Figs. 2a, b) and the absence of a clear thermodynamic
 378 advantage during the intensification period. Therefore, these SST patterns likely played a
 379 secondary role compared to the dynamically driven processes, such as enhanced vorticity
 380 advection and upper-level divergence.

381 This supports the notion that SSTs, in this case, provided a necessary but not sufficient
 382 condition for RI. The findings from Bister and Emanuel (2002) and Fischer et al. (2019)
 383 reinforces this view by emphasizing that, without favorable upper-level forcing and
 384 adequate storm structure, warm SSTs alone are insufficient to trigger RI, even when PI
 385 values appear theoretically consistent.

386



387
 388 Figure 3. (a-f) SST SCC difference maps (P_{80} - P_{20} ensembles; °C) for selected time steps from
 389 +10 h to +60 h. Dots indicate regions where differences are statistically significant at the 95%
 390 confidence level.
 391

392 3.2 Trough interaction and TC rapid intensification

393
 394 **Since SST fail to explain the differences observed** among the ensemble members in Lidia's
 395 intensification, we examine the mid- and upper-level dynamic environment. Figure 4 shows
 396 the eastward progression of a trough in both ensemble groups. The trough is notably
 397 broader in the P_{80} -ensemble, particularly from time step +55 h. At 250 and 300 hPa (Figs.
 398 4a, b), the isohypses in the P_{80} -ensemble exhibit substantial deformation toward Lidia. The
 399 trough deepens further at 500 hPa (Fig. 4c), extending southward to approximately 20°N.
 400 This southward intrusion brings the trough into closer proximity with the tropical cyclone,
 401 especially in the RI ensemble members, where a more pronounced elongation is observed.

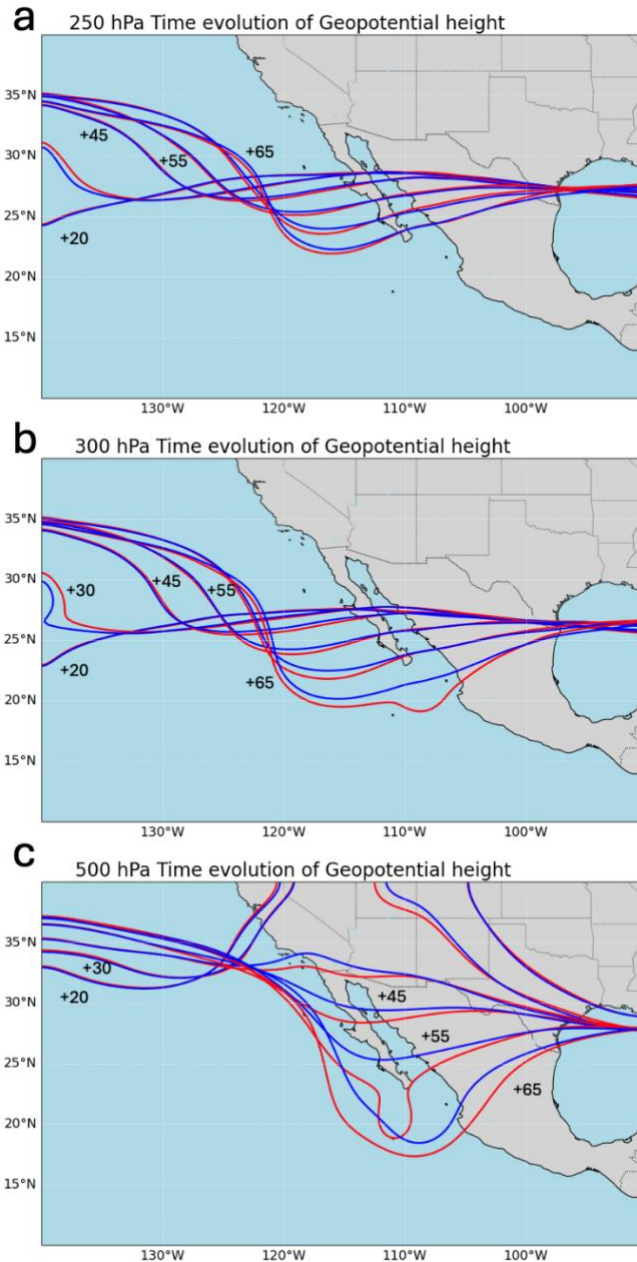
402 This configuration likely favored a moist and unstable environment ahead of the cyclone,
403 while simultaneously enhancing vorticity advection and synoptic-scale ascent.

404

405 Such a configuration is consistent with previous findings on optimal trough–tropical cyclone
406 interactions (e.g., Hanley et al., 2001; Fischer et al., 2019), which suggest that intensification
407 is favored when the trough approaches from the northwest at an appropriate distance.
408 Although Fischer et al. (2019) noted that narrower upper-tropospheric troughs may be more
409 conducive to RI, the enhanced interaction observed here may result from the deeper and
410 more equatorward positioning of the broader trough in the RI group (particularly at +45 h
411 and +55 h in Fig. 4c). Additionally, although our analysis focused primarily on dynamical
412 variables, we acknowledge that mid-level tropospheric humidity, particularly the intrusion
413 of dry air, may also have influenced the timing or suppression of RI in some ensemble
414 members, as highlighted in recent work by Fischer et al. (2023). **A more detailed analysis of
415 the humidity and ventilation effects is presented later sections.**

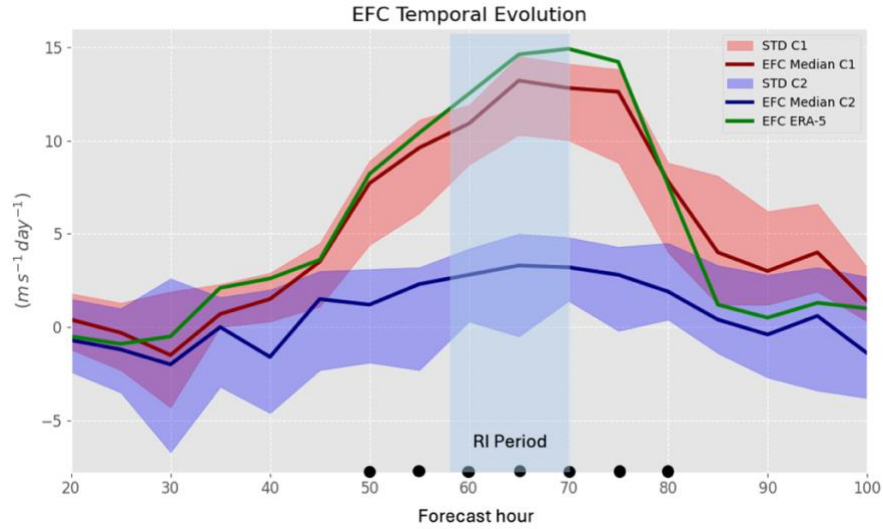
416

417 The EFC is computed to diagnose the trough-TC interaction in Hurricane Lidia. The
418 results indicate that P_{80} -ensemble exhibits significantly higher EFC values compared to the
419 P_{20} -ensemble group. These differences begin to emerge around +40 h and become
420 significant between +50 h and +80 h just before and during Lidia RI period (Fig. 5),
421 suggesting that enhanced EFC may have contributed to the onset and maintenance of
422 RI in the P_{80} members. P_{80} -ensemble is closely aligns with ERA5 reanalysis (exceeding
423 $10 \text{ m s}^{-1} \text{ day}^{-1}$ during RI period). These elevated EFC values are consistent with the
424 findings of DeMaria et al. (1993) for the North Atlantic basin, where EFC values greater than
425 $10 \text{ m s}^{-1} \text{ day}^{-1}$ serve as an indicator of a trough-TC interaction. Therefore, the obtained
426 EFC values highlight a strong interaction between Lidia and the trough, suggesting that
427 dynamic forcing, estimated using a QG diagnostic framework, specifically the Trenberth
428 formulation enhances vertical motion and may contribute to upper-level divergence,
429 potentially triggering RI. This behavior in the Pacific is analogous to the quasi-stationary
430 effect of the tropical upper tropospheric trough (TUTT) in the Caribbean, previously
431 analyzed by Sanders (1975). However, unlike the Caribbean TUTT, which tends to be more
432 persistent and conducive to cyclogenesis, the trough interacting with Hurricane Lidia in the
433 Pacific was transient and engaged with an already mature TC. While we do not explore track
434 changes in detail here, prior analyses suggested that this synoptic feature may have also
435 influenced Lidia's trajectory in earlier initializations. Nonetheless, our focus remains on the
436 intensification phase. These types of interactions are particularly relevant for hazard
437 assessment, as they can increase the risk for densely populated areas in Mexico during late
438 summer, when TCs are most frequent in the eastern Pacific basin (López-Reyes and
439 Meulenert, 2021).



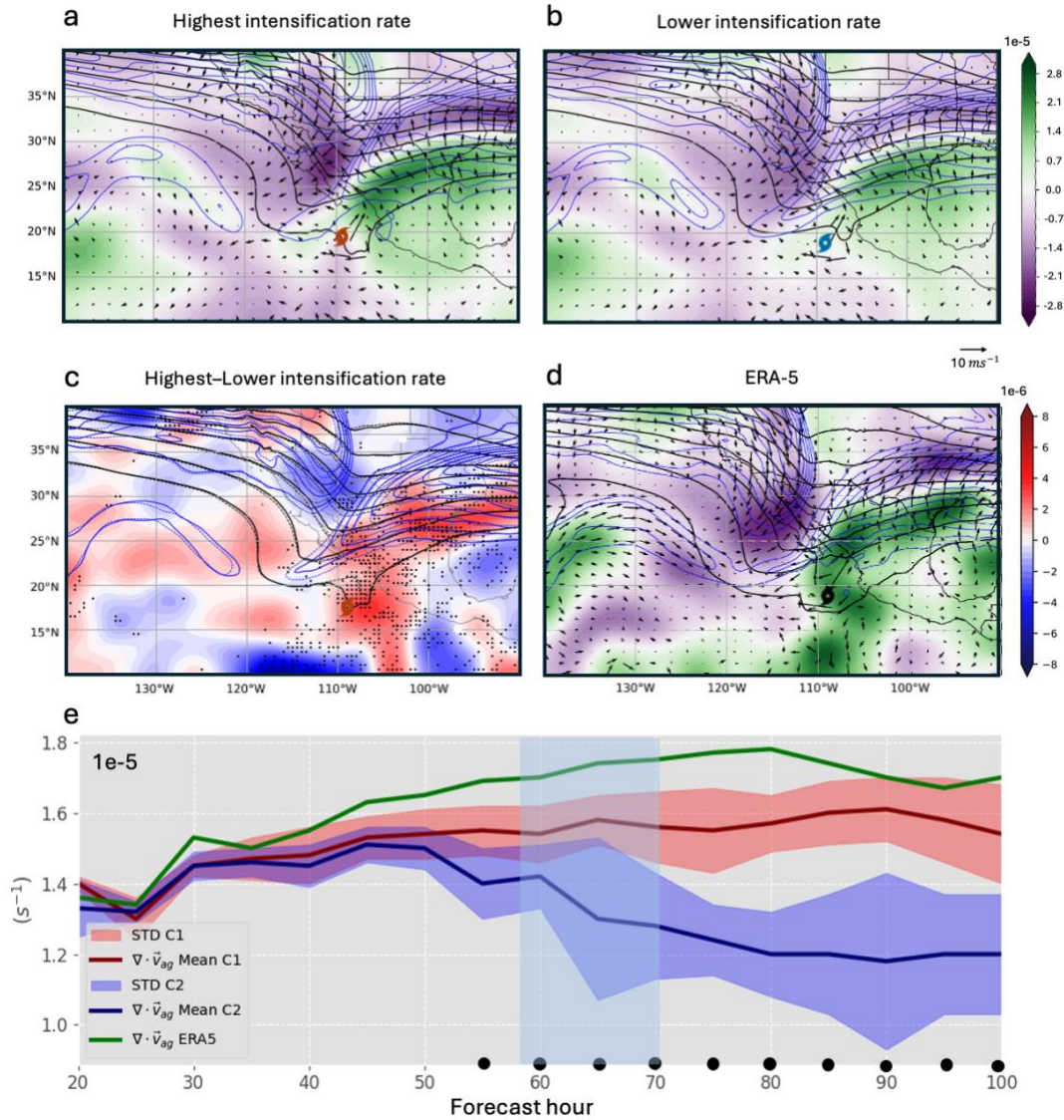
440
 441 Figure 4. Z Composite corresponding to the highest (red contours) and lower (blue contours)
 442 IRG, at (a) 250 hPa, (b) 300 hPa and (c) 500 hPa, before and during the trough-TC interaction.
 443

444 To assess the dynamical processes supporting Lidia's intensification, EPS outputs during the
 445 RI period are compared with ERA5 fields. Although quasi-geostrophic diagnostics are
 446 typically applied in extratropical contexts, this approach is particularly relevant in the
 447 northeastern Pacific, where the presence of the subtropical jet during the boreal autumn
 448 increases the likelihood of TC-subtropical jet stream (Hanley et al., 2001). These
 449 interactions can play a key role in TC intensification and recurvature, especially in a
 450 region where high-resolution forecasts remain limited.



451
 452 Figure 5. EFC temporal evolution calculated within a radial range of 300 to 600 km at 250
 453 hPa, with the red (blue) line representing the higher (lower) IRG. The red (blue) shaded
 454 regions indicate the STD for the highest (lower) IRG, green line represents the EFC based on
 455 ERA5 data and dots indicate statistical significance.

456
 457 In Figures 6a and 6b, the $\nabla \cdot \vec{V}_{ag} > 0$ values, associated with the trough and jet streak,
 458 are located to the northeast of Lidia. This configuration strongly favors enhanced upper-level
 459 divergence over Lidia and acts as a mechanism that drives upward motions. The quasi-
 460 geostrophic $\nabla \cdot \vec{V}_{ag}$ is notably higher in P_{80} than in P_{20} -ensemble (Fig. 6a-c); P_{80} -ensemble
 461 closely matches ERA5 across nearly all regions surrounding Lidia (Fig. 6d), suggesting a
 462 stronger forcing induced by the interaction with the trough and jet streak.
 463



464

465 Figure 6. $\nabla \cdot \vec{V}_{ag}$ -Composite (shaded; s^{-1}), jet stream (blue contours at 10 ms^{-1} intervals)
 466 and Z at 250 hPa (black contours at 20 m intervals) of (a) P_{80} , (b) P_{20} IRG (c) $P_{80} - P_{20}$ of
 467 $\nabla \cdot \vec{V}_{ag}$ (shaded; dots indicated statistical significance), solid (dashed) contour represent Z
 468 of P_{80} (P_{20}) IRG, and (d) same for ERA5 data. e) $\nabla \cdot \vec{V}_{ag}$ Temporal evolution calculated within
 469 a radial range of 500 km at 250 hPa, with the red (blue) line representing the higher (lower)
 470 IRG. The red (blue) shaded regions indicate the STD for the highest (lower) IRG and dots
 471 indicate statistical significance.

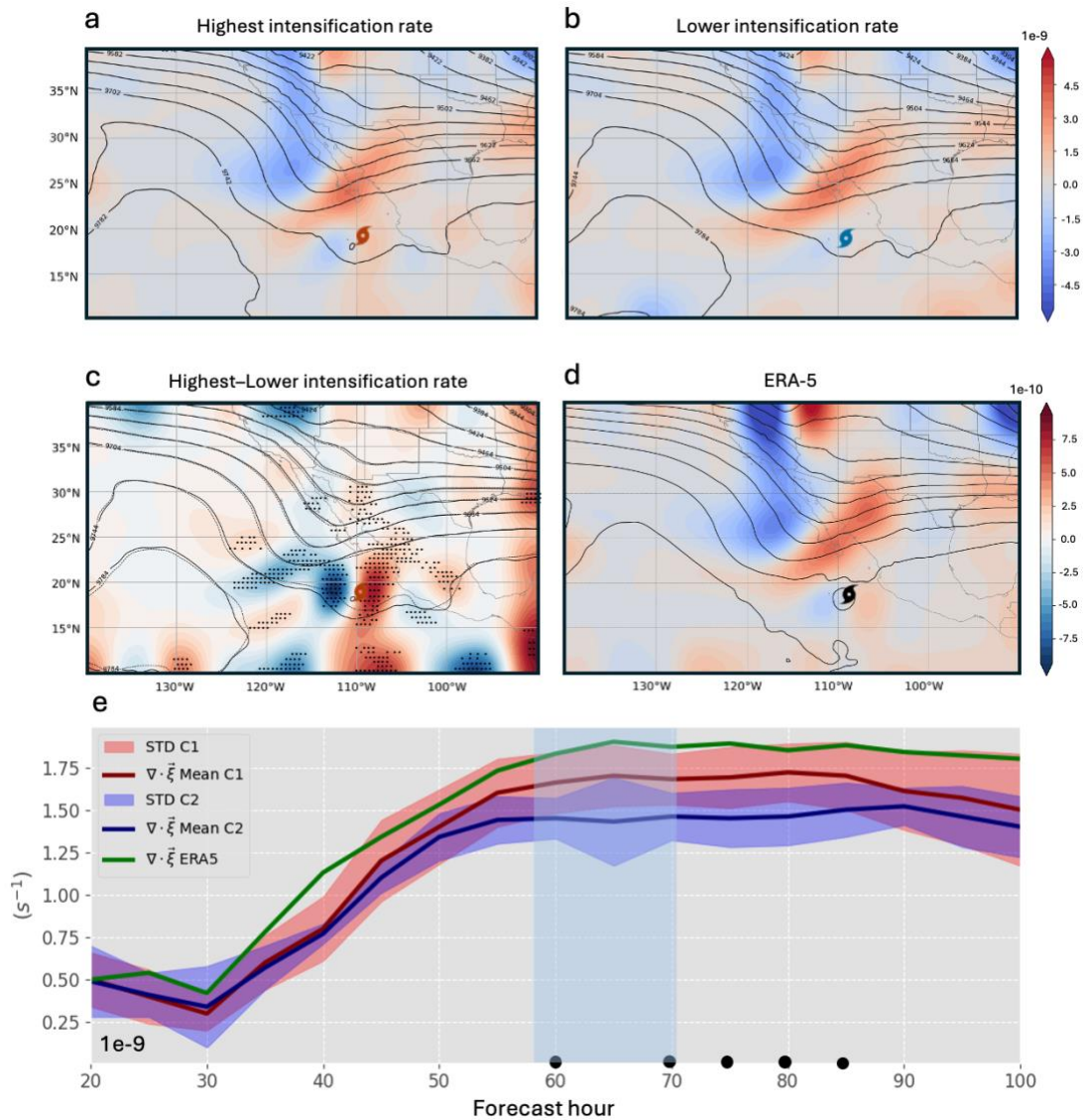
472

473

474 Figure 6e reveals distinct differences in the evolution of ageostrophic divergence
 475 between the two ensemble groups. The P_{80} -ensemble shows consistently higher values of
 476 ageostrophic divergence, particularly between +50 and +75 h, coinciding with Lidia's RI
 477 period. In contrast, the P_{20} -ensemble exhibits lower and declining values during this period,
 indicating weaker dynamical forcing. ERA5 closely follows the P_{80} -ensemble pattern,

478 supporting the physical credibility of the ensemble signal. These results highlight the role of
479 upper-level divergence and jet-induced ascent in supporting RI in the P_{80} -ensemble.
480

481 According to the quasi-geostrophic theory, regions with positive (negative) vorticity
482 advection are associated with upward (downward) vertical motions (Bluestein, 1992). In
483 Figures 7a and 7b, $\vec{V} \cdot \nabla(\vec{\xi} + f)$ is associated with a trough configuration, depicting
484 predominant positive (negative) values in front (behind) of the trough axis. In the same way,
485 $\vec{V} \cdot \nabla(\vec{\xi} + f)$ shows stronger and statistically significant positive values near Lidia's position
486 in P_{80} compared to P_{20} -ensemble (Fig. 7c); in addition, a branch with positive vorticity
487 advection values around Lidia is only identified in P_{80} -ensemble, and similar to ERA5 (Fig.
488 7d). The above is consistent with the greater proximity of the trough to Lidia in P_{80} -
489 ensemble, highlighting a more intense cyclonic vorticity advection over Lidia (also at earlier
490 time steps; not shown). However, we acknowledge that part of this signal also reflects the
491 contribution from the TC circulation itself. Nonetheless, at the synoptic scale, coherent
492 differences associated with the trough's position and structure are clearly discernible
493 between ensemble groups. Therefore, the trough-TC interaction is more robust in P_{80} than
494 in P_{20} as indicated earlier with the EFC metric. This finding shows that a mid- and upper-
495 levels trough can facilitate the development of a moist layer (Wu et al., 2015), contributing
496 to Lidia intensification.
497



498
 499 Figure 7. $\vec{V} \cdot \nabla(\xi + f)$ -Composite (shaded; s^{-2}) and Z at 300 hPa (black contours at 20 m
 500 intervals) of (a) the P_{80} (b) P_{20} IRG, (c) $P_{80} - P_{20}$ (shaded; dots indicated statistical
 501 significance), solid (dashed) contour represent Z of P_{80} (P_{20}) IRG and (d) same for ERA5 data.
 502 e) $\vec{V} \cdot \nabla(\xi + f)$ Temporal evolution calculated within a radial range of 500 km at 500 hPa,
 503 with the red (blue) line representing the higher (lower) IRG. The red (blue) shaded regions
 504 indicate the STD for the highest (lower) IRG and dots indicate statistical significance.
 505

506 Figure 7e confirms the stronger vorticity forcing in the P_{80} -ensemble throughout Lidia's
 507 intensification period. From time step +40 h onward, the P_{80} group exhibits consistently
 508 higher values of vorticity advection, peaking near the RI window (+55 to +70 h), while the
 509 P_{20} group remains consistently weaker, with little variability. The ERA5 line again follows the
 510 P_{80} trajectory, supporting the robustness of the dynamical signal. The statistically significant
 511 differences suggest that enhanced cyclonic vorticity advection, likely associated with the
 512 trough's mid- and upper-levels deformation, played a crucial role in promoting upward
 513 motion and intensification in the P_{80} -ensemble.

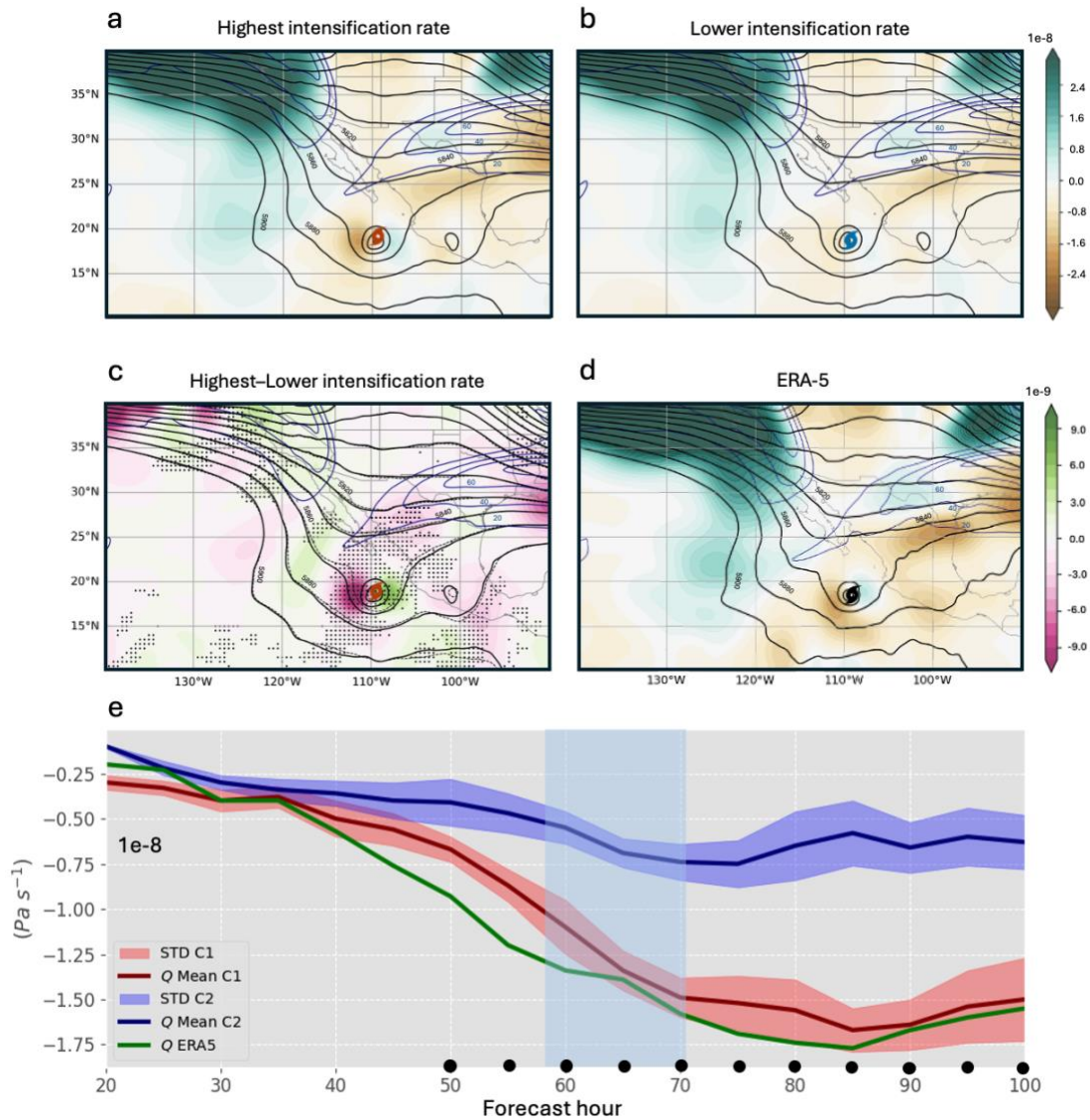
514 The Q field in the P_{80} -ensemble (Fig. 8a) shows a more intense upward forcing in the
515 right region of the trough and extending to the divergence zone at the right entrance of the
516 jet streak in comparison to P_{20} Q values (Fig. 8b). We selected the 500 hPa level because
517 this level exhibited stronger trough elongation and clearer interaction with the TC. This
518 contrast becomes even more evident when considering only RI members within P_{80} -
519 ensemble (Figs. 9 and Fig. A3 in Appendix) are selected and reinforces the idea of the
520 influence of the trough in Lidia's RI. Based on Eq. (1), negative values of the forcing term Q
521 correspond to regions of upward vertical motion induced by vorticity advection via the
522 thermal wind (Dostalek, 2012). The areas surrounding Lidia are strongly influenced by the
523 dynamical forcing induced by the trough and the jet streak in the P_{80} -ensemble (Fig. 8c and
524 Fig. A3 in Appendix). It is worth noting that the QG ascent patterns near the TC center may
525 partially reflect contributions from the TC's own circulation. This implies that some
526 contamination from the TC's inner-core vorticity cannot be completely ruled out. To assess
527 this, we performed an additional localized filtering applied exclusively to the TC circulation,
528 which effectively removes most of the mesoscale contribution of the vortex. As shown in
529 Appendix A3, the resulting Trenberth forcing field reveals a clearer synoptic-scale signal
530 associated with the trough and the jet-streak interaction, supporting that the large-scale
531 forcing dominates despite minor contamination near the TC center.

532

533 This result is further supported by the ERA5 reanalysis data (Fig. 8d), which reveals a Q
534 pattern similar to that observed in the P_{80} -ensemble, but with greater intensity (note that
535 ERA5 is only a member, not a composite group). In the absence of substantial
536 thermodynamic differences (Figs. 2 and 3), these results highlight the dominant role of
537 dynamic interaction between the trough, the jet streak, and the cyclone during RI. However,
538 we acknowledge that tropospheric moisture, particularly the intrusion of mid-level dry air,
539 may also have influenced the timing or suppression of RI in some members, as suggested by
540 Fischer et al. (2023). These findings are particularly relevant for operational forecasting, also
541 demonstrating the capability of the ECMWF EPS to simulate Lidia's RI, even under complex
542 extratropical interactions influences.

543

544 The temporal evolution of the Trenberth forcing (Fig. 8e) reveals a clear and consistent
545 signal in the P_{80} -ensemble, with significantly more negative values, indicative of stronger
546 synoptic-scale upward motion. This enhanced forcing begins slightly before the onset of
547 Lidia's RI (which starts around +55 h), with statistically significant differences emerging at
548 approximately +50 h, and peaks between +50 and +70 h. This temporal analysis supports a
549 causal interpretation, suggesting that the synoptic-scale dynamical forcing likely contributed
550 to initiating the RI process, rather than being a consequence of it. In contrast, the P_{20} -
551 ensemble shows much weaker and less coherent values throughout, indicating and absence
552 of favorable dynamical support for RI.

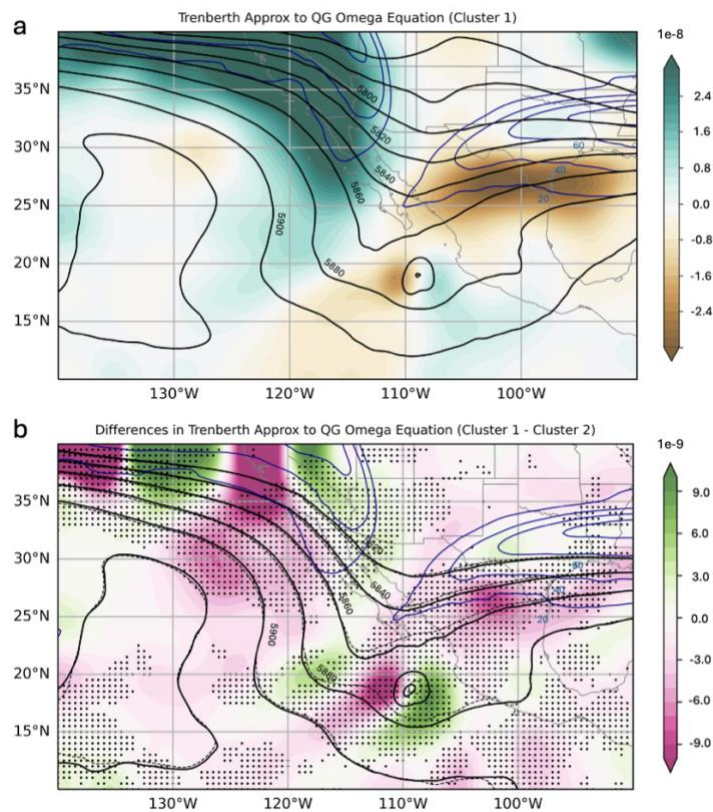


553
 554 Figure 8. Q -Composite (shaded; $Pa \cdot s^{-1}$) at 500 hPa, jet stream (blue contours at $10 m s^{-1}$
 555 intervals) at 250 hPa and Z at 500 hPa (black contours at 20 m intervals) of (a) the P_{80} (b)
 556 P_{20} IRG, (c) $P_{80} - P_{20}$ of Q (shaded; dots indicated statistical significance), solid (dashed)
 557 contour represent Z of P_{80} (P_{20}) IRG and (d) same for ERA5 data. (e) Q Temporal evolution
 558 calculated within a radial range of 500 km at 500 hPa, with the red (blue) line representing
 559 the higher (lower) IRG. The red (blue) shaded regions indicate the STD for the highest (lower)
 560 IRG and dots indicate statistical significance.

561

562 In P_{80} -ensemble, the trough is broader at Lidia's latitude, we found a difference of
 563 ≈ 300 km between the continuous and dashed contours and positioned closer to Lidia
 564 (around 500 km; Figs. 3a, b), in agreement with previous studies showing that favorable
 565 trough-TC interactions occur when the trough lies to the northwest at an optimal distance
 566 (Hanley et al., 2001). Significant differences are observed in both the amplitude and distance
 567 relative to Lidia (Fig. 2c). A similar pattern has been noted in some Atlantic basin cases
 568 (Hanley et al., 2001; Fischer et al., 2019; Sato et al., 2020), where effective trough-TC

569 interactions are facilitated by a favorable distance, typically between 500-1000 km.
 570 However, Fischer et al. (2019) found that northwestward-approaching troughs were
 571 associated with the lowest rates of RI among the configurations they examined, with
 572 stronger intensification occurring when a cutoff low was located to the southwest of the TC.
 573 While Lidia's interaction does not fully match this optimal configuration, the proximity and
 574 orientation of the trough in the RI group (Fig. 3a) still suggest a dynamically favorable setup,
 575 compared to the less aligned structure seen in the non-RI group (Fig. 3b). **Although the TC**
 576 **itself may contribute to modifying the trough structure in the P_{80} -ensemble, it is noteworthy**
 577 **that a broader and deeper trough is already evident from the early forecast hours (see Fig.**
 578 **4), suggesting a pre-existing synoptic configuration conducive to stronger TC–trough**
 579 **interaction.**
 580



581

582 Figure 9. (a) Q -Composite (shaded; $Pa \cdot s^{-1}$) at 500 hPa, jet stream (blue contours at
 583 $10 m s^{-1}$ intervals) at 250 hPa and geopotential height at 500 hPa (black contours at 20 m
 584 intervals) of RI members, (b) Trenberth forcing (shaded) differences (P_{80} -RI members
 585 minus P_{20} ; dots indicated statistical significance), solid (dashed) contour represent
 586 geopotential height of RI group.

587

588 These findings further support the hypothesis that dynamical forcing triggered Lidia's
 589 RI. In the P_{80} -ensemble the trough is broader (~ 300 km) and closer to Lidia (~ 500 km; Figs.
 590 10a, b). Evident differences are observed in both the amplitude and distance relative to Lidia
 591 (Fig. 10c). A similar configuration has been noted in some Atlantic basin cases (Hanley et al.,

592 2001; Fischer et al., 2019; Sato et al., 2020), where effective trough–TC interactions require
593 a favorable distance. This configuration is associated with different behavior of \vec{V}_{irr} at upper-
594 levels (Figs. 10d-f), where the proximity of the trough’s divergence zone enhances
595 evacuation mass in the P_{80} -ensemble (Fig. 10d) with significant \vec{V}_{irr} differences reaching
596 $\sim 4 \text{ ms}^{-1}$ to the west-northwest of Lidia. Consequently, the superposition of both
597 divergence zones amplifies the upper-level anticyclonic circulation, consistent with
598 increasing EFC values in P_{80} -ensemble toward Lidia (Fig. 5) strengthens upward motion and
599 enabling RI.

600

601 On the other hand, the VWS remains moderate around Lidia’s center in both ensemble
602 groups, with values between $10\text{--}15 \text{ ms}^{-1}$ during RI period (Fig. 10g, h). Slightly higher VWS
603 values are observed to the south of Lidia. To the west and near of Lidia center, VWS values
604 are higher in P_{80} -ensemble (around $\sim 5 \text{ ms}^{-1}$; Fig. 10i), though still within favorable ranges
605 for intensification (Sharma and Varma, 2022). In contrast, regions beyond 2° radial distance
606 in P_{80} -ensemble show significantly lower VWS values, consistent with the position and
607 shape of the jet stream. In P_{20} -ensemble, a stronger jet stream is present north of Lidia,
608 resulting in a more significant increase in VWS compared to P_{80} -ensemble. Thus, the
609 position and intensity of the jet streak relative to Lidia’s position could potentially limit its
610 intensification in P_{20} -ensemble.

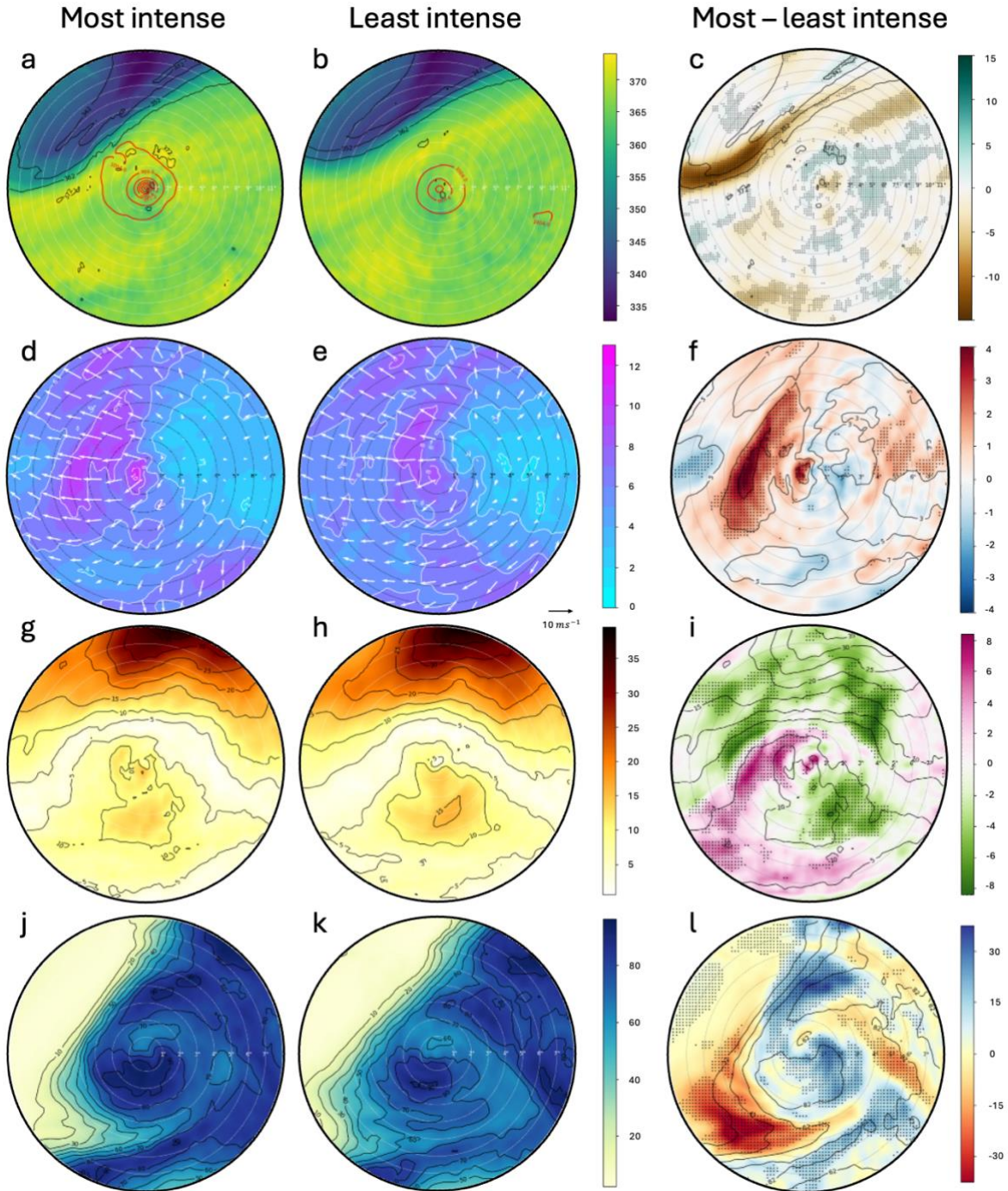
611

612 The results suggest that the upward motions induced by dynamical mechanisms
613 associated with Lidia’s interaction with a trough are consistent with the greater RH in P_{80} ,
614 particularly near the center of Lidia and in the southern region where the trough appears to
615 enhance its influence (Figs. 10j–l). This region coincides with the trough-cyclone interaction,
616 where vertical motions are strongly driven by dynamical forcing. Additional checks
617 performed for forecast hours prior and during to RI already showed discernible differences
618 in RH between both ensembles, with higher mid-tropospheric humidity in P_{80} -ensemble
619 compared to the weak-intensifying members. The analyzed atmospheric patterns, including
620 the dynamical forcing associated with the trough and jet streak, suggest that higher RH in
621 P_{80} may be linked to increased condensation rates during air ascents around center of
622 Hurricane Lidia, leading to core warming (Emanuel, 1986; Zhang et al., 2013; Zhang and
623 Emanuel, 2016). A moister mid-tropospheric environment can also suppress the intrusion
624 of dry air, reduce ventilation and allow convection to remain deeper and more symmetric
625 (Tang and Emanuel, 2010, 2012; Riemer et al., 2010; Ge et al., 2013). The enhanced latent
626 heat release in such a moist environment strengthens the warm core and facilitates a **greater**
627 **and improved divergence in height, which facilitates the evacuation of mass from the core**
628 **of the TC and favors a sustained ascent**. This supports a **more efficient upper-level outflow**,
629 effectively mitigating the detrimental influence of environmental VWS (Rios-Berrios and
630 Torn, 2017; Qiu et al., 2020).

631

632 Specifically, the reduction in VWS observed in the P_{80} -ensemble **reflects a weakening**
633 **of the environmental vertical wind gradient** over the storm core. This occurs as the
634 interaction with the upper-level trough enhances mass divergence aloft, weakening the
635 upper-level winds immediately above the cyclone. Simultaneously, stronger and more

636 vertically aligned convection, sustained by the higher mid-tropospheric humidity, reinforces
637 the upper-level outflow and reorganizes the wind field around the vortex, effectively
638 reducing the shear acting on the inner core (Riemer and Montgomery, 2011; Ge et al., 2013;
639 Tang and Emanuel, 2012; Ryglicki et al., 2019). This process illustrates how the moist
640 environment can offset the detrimental influence of environmental shear **by reducing**
641 **ventilation and enabling greater vertical mass flux within the TC core (Alland et al., 2021)**,
642 rather than by promoting a more efficient coupling between the outflow and the ambient
643 flow (Figs. 10g–l and Figs. 11c, d). Therefore, the observed reduction in shear is better
644 understood as a localized, dynamically and thermodynamically mediated adjustment rather
645 than a broad environmental change. Together, higher RH, reduced ventilation, and
646 enhanced synoptic-scale forcing acted synergistically to precondition the vortex and create
647 an optimal environment for rapid intensification in the P_{80} -ensemble.
648



649
 650
 651
 652
 653
 654
 655
 656
 657

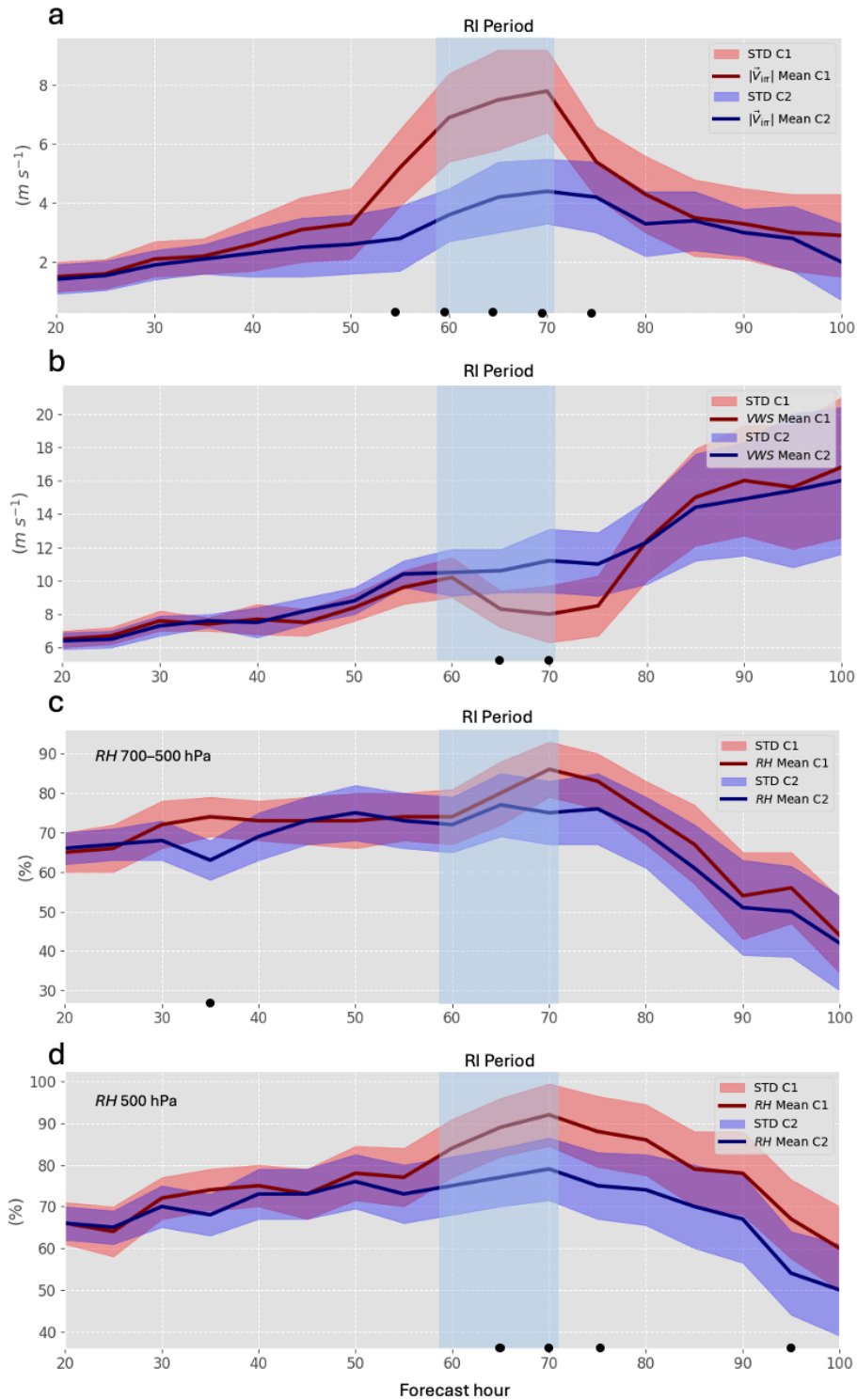
Figure 10. SCC for the time step 55-h of: θ (K) at 1.5 PVU for (a) P_{80} , (b) P_{20} IRG, and (c) $P_{80} - P_{20}$ IRG, red contours are MSPL; $|\vec{V}_{irr}|$ ($m s^{-1}$), at 200 hPa for (d) P_{80} , (e) P_{20} IRG, and (f) $P_{80} - P_{20}$ IRG; VWS ($m s^{-1}$; between 0-500 km radius) for (g) P_{80} , (h) P_{20} IRG and (i) $P_{80} - P_{20}$ IRG, and RH (%) (j) P_{80} , (k) P_{20} IRG and (l) $P_{80} - P_{20}$ IRG at 500 hPa. Each concentric ring in the panels corresponds to 1° radius, and the outermost circle representing the SCC domain has a radius of 8°

658 While the mean RH differences between the P_{80} - and P_{20} -ensembles were modest in
659 magnitude, Figure 10l reveals statistically significant anomalies of approximately 10% near
660 the storm center and along its southern flank. These regions of enhanced mid-tropospheric
661 moisture likely played an active role in sustaining deep convection and facilitating the
662 vertical alignment of the vortex, consistent with the stronger and more organized convective
663 structure observed in the P_{80} -ensemble. This behavior is in agreement with previous studies
664 (e.g., Alland et al., 2021; Tang and Emanuel, 2010), which demonstrated that higher mid-
665 level humidity reduces ventilation and supports the maintenance of deep, symmetric
666 convection even under moderate vertical wind shear.

667
668 Similarly, Hamaguchi and Takayabu (2021) described how upper-level dynamical forcing
669 can induce synoptic-scale ascent that moistens the mid–upper troposphere prior to
670 convective amplification in tropical disturbances. A comparable sequence is evident in the
671 P_{80} -ensemble, where enhanced negative Trenberth forcing and upper-level divergence
672 preceded a significant increase in mid-level relative humidity during the rapid intensification
673 period (Fig. 11c, d). This correspondence reinforces the interpretation that upper-level
674 dynamical ascent and mid-tropospheric moistening acted together to precondition the
675 environment for RI in the P_{80} -ensemble.

676
677 Instead, the P_{80} -ensemble is characterized by early and sustained dynamic forcing,
678 particularly the strong negative Trenberth forcing observed before the RI onset, which likely
679 initiated upward motion and enhanced upper-level mass divergence near the storm core.
680 This synoptic-scale ascent, coupled with the release of latent heat, contributed to a
681 favorable adjustment of the potential vorticity structure in the upper troposphere,
682 reinforcing the outflow and aiding in the vertical alignment of the vortex. Consequently, the
683 observed reduction in VWS in P_{80} -ensemble can be interpreted as a combined result of both
684 dynamic and thermodynamic processes acting in phase, rather than as a purely dynamical
685 outcome. This reduction is related to higher Trenberth forcing, supporting a causal sequence
686 in which synoptic-scale forcing preconditions, such as strong convection and vortex
687 alignment, subsequently amplify this favorable state, accelerating the intensification
688 process (Chen and Gopalakrishnan, 2019; Komaromi and Doyle, 2018; Stevenson et al.,
689 2014). Figure 11 confirms this evolution: stronger divergence and PV anomalies emerge
690 after the initial forcing, aligning with the onset of RI. The combined evidence supports the
691 conclusion that in the case of Hurricane Lidia, RI was dynamically triggered by the
692 interaction with the upper-level trough and jet stream, while thermodynamic factors such
693 as PI, SST, and RH acted in concert with the dynamical forcing, serving as supportive
694 components that enhanced the overall efficiency of the intensification process.

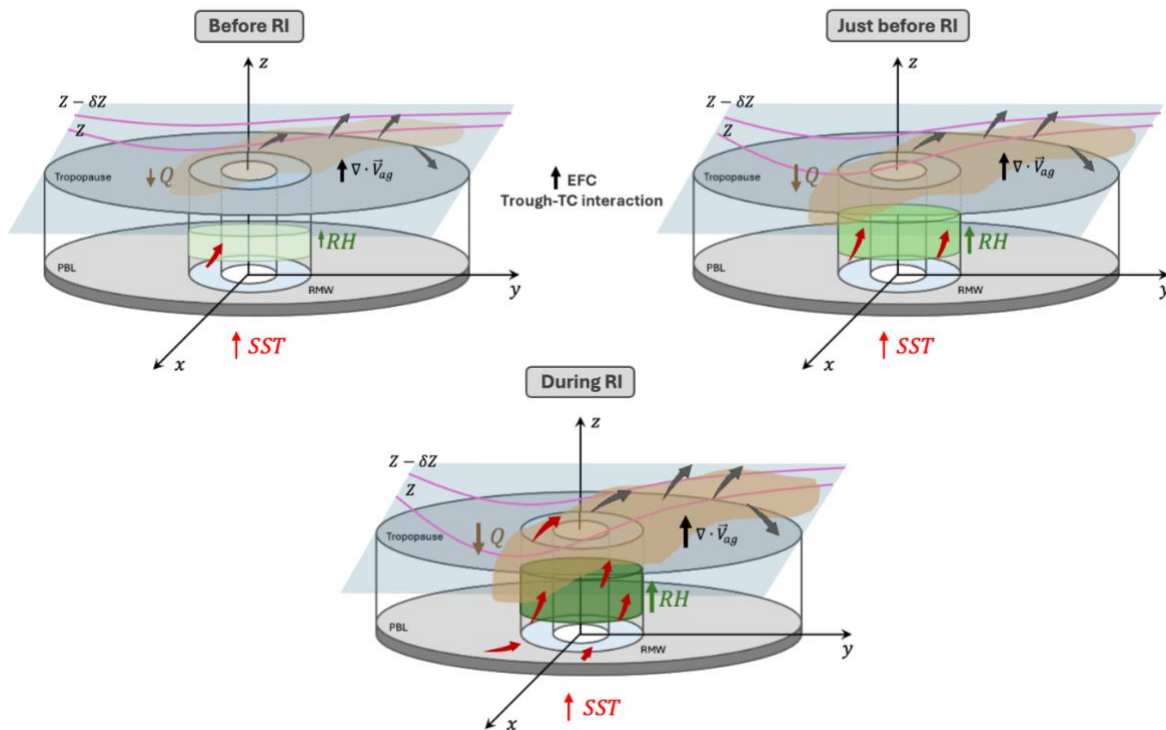
695



696
697
698
699
700
701

Figure 11. Time evolution of (a) ageostrophic wind at 250 hPa, (b) VWS (850–200 hPa), (c) RH (700–500 hPa) and (d) RH (500 hPa) within 500 km of Lidia. Red (blue) lines show the mean for the higher (lower) IRG; shaded areas indicate STD. Light blue band indicate the RI period. Black dots denote significant differences.

702 To better connect the individual diagnostics discussed in this study, Figure 12 presents a
 703 conceptual schematic summarizing the key mechanisms acting before, at the onset, and
 704 during Lidia’s RI. The illustration integrates the main results: (i) the approach and
 705 deformation of the upper-level trough, (ii) the strengthening of synoptic-scale ascent
 706 diagnosed through negative Trenberth forcing, (iii) the increase in upper-level divergence
 707 and cyclonic vorticity advection, (iv) the moistening of the mid-troposphere, and (v) the
 708 subsequent reduction of VWS and enhancement of the upper-level outflow. This schematic
 709 encapsulates how the combination of dynamic forcing and favorable thermodynamic
 710 conditions preconditioned and then accelerated the intensification process in the P_{80} -
 711 ensemble in this case of study.
 712



713
 714 Figure 12. Schematic overview of the dynamical and thermodynamic processes leading to
 715 Hurricane Lidia’s RI. Before RI, the mid-level trough induces increasing dynamical forcing and
 716 weak ascent near the cyclone. Just before RI, enhanced negative Trenberth forcing (**shaded**
 717 **region in brown**) strengthens upper-level divergence (**gray arrows**) and mid-tropospheric
 718 moistening (**light green cylinders**). During RI, the interaction between the trough and the
 719 vortex maximizes ascent (**red arrows**), increases RH (**green cylinder**), and combines with
 720 elevated SST to support a deep, vertically aligned convective core.

721
 722 **4 Summary and conclusions**

723
 724 This research presents a novel examination of the interaction between a mid- and
 725 upper-level trough and Hurricane Lidia in the northeastern Pacific, a region where studies
 726 are less frequent compared to the Atlantic basin, particularly regarding RI. Since
 727 thermodynamic factors such as PI and SST do not seem to explain the differences observed

728 between the members of the group in the intensification of Lidia, some dynamic variables
729 associated with forcings more typical of higher latitudes are analyzed, which usually appear
730 in the autumn months in subtropical areas of the northeastern Pacific coasts (DiMego et al.,
731 1976).

732

733 Based on previous work in the Atlantic basin (Fischer et al., 2019), which demonstrated
734 that TCs experiencing RI often coincide with the presence of an upper-level trough
735 approaching from the northwest at an optimal distance, our study expands this framework
736 by demonstrating for the first time a similar dynamic configuration driving RI in the
737 northeastern Pacific. By analyzing synoptic dynamical indicators, such as the Trenberth
738 forcing, ageostrophic wind divergence and vorticity advection, we demonstrate how these
739 dynamical processes play a crucial role in Lidia's RI. The EFC values greater than 10
740 $ms^{-1}day^{-1}$ in the P_{80} -ensemble indicate the trough-TC interaction during the RI period,
741 reinforcing the critical role of the trough in enhancing vertical motions and upper-level
742 divergence. In a context where ocean temperatures are rising and an increasing trend in RI
743 hurricane frequency has been documented (Majumdar et al., 2023; Li et al., 2023), this
744 work provides the first case study of trough-TC interaction leading to RI in the northeastern
745 Pacific, highlighting the increased proximity and breadth of the trough near Lidia a key driver
746 of its RI. Unlike Fischer et al. (2019), who focused on climatological composites and
747 individual case diagnostics in the Atlantic, this study provides a probabilistic ensemble-
748 based assessment linked to dynamic forcings under realistic forecast uncertainty conditions.

749

750 The obtained results underscore the role of dynamical mechanisms, analyzed through
751 quasi-geostrophic forcing, in triggering significant upward vertical motions that contribute
752 to the Lidia's RI. These dynamics are evident in the P_{80} -ensemble (even more evident in RI
753 members), where Lidia undergoes RI, showing stronger ageostrophic wind divergence,
754 enhanced vorticity advection at mid- and upper-levels, and more pronounced Trenberth
755 forcing, all associated with the influence of the trough (Fig. 12). In contrast, in the P_{20} -
756 ensemble, the trough is still present but its interaction with Lidia appears less favorable,
757 characterized by weaker dynamical coupling and a less optimal alignment between the
758 trough axis and the cyclone center. The proximity and intensity of a jet stream to Lidia's
759 north increase in VWS, which limited the potential for intensification.

760

761 The enhanced Trenberth forcing in the P_{80} -ensemble appears several hours before the
762 onset of RI, indicating that synoptic-scale ascent likely preconditioned the environment
763 rather than resulting from the intensification itself. This timing supports a causal
764 interpretation in which the large-scale forcing drives changes within the TC. Following this
765 initial dynamic trigger, latent heat release near the cyclone core contributed to a favorable
766 upper-level PV redistribution. This adjustment likely enhanced the upper outflow layer and
767 contributed to the subsequent reduction in VWS observed in the P_{80} group, further
768 amplifying the intensification process.

769

770 On the other hand, although the mean relative humidity differences between the two
771 ensembles were modest, a closer inspection revealed locally enhanced mid-tropospheric

772 moisture near the storm center and along the southern sector of Lidia, where the trough
773 influence was strongest. This moisture distribution likely contributed to sustaining deep
774 convection and mitigating mid-level ventilation of low-entropy air, **allowing the vortex to**
775 **remain vertically aligned and more resistant to environmental shear** (Riemer and
776 Montgomery, 2011; Tang and Emanuel, 2012; Ge et al., 2013). Therefore, while the synoptic-
777 scale dynamic forcing acted as the primary trigger for upward motion and potential vorticity
778 redistribution, the accompanying moist environment played a complementary role by
779 enhancing latent heat release and reducing the effective VWS over the cyclone core. In this
780 sense, RH acted not merely as a passive background condition but as a cooperative
781 thermodynamic factor that amplified the impact of the dynamic forcing, ultimately
782 supporting the RI observed in the P_{80} -ensemble.

783
784 By demonstrating the effectiveness of EPS-ECMWF in capturing complex trough-TC
785 interactions, this study highlights the critical role of EPS as an indispensable tool for
786 operational forecasting in the northeastern Pacific, especially along the Pacific coast of
787 Mexico. EPS are particularly valuable for quantifying uncertainty in RI scenarios, which
788 remain challenging to predict due to the complex dynamical and thermodynamical
789 processes involved. The present results show that EPS can successfully differentiate
790 between dynamically favorable and unfavorable environments, even in a context where
791 high-resolution operational models are not readily available, as is often the case in Mexico.
792 This makes EPS-based diagnostics especially useful for forecasters operating in data-sparse
793 or resource-limited settings. In this region, during autumn months, the subtropical jet
794 stream frequently interacts with TCs, increasing the likelihood of dynamical forcing
795 mechanisms that can either enhance or inhibit intensification.

796
797 This study illustrates how broader and deeper mid-level troughs, such as the one
798 observed at 500 hPa in Hurricane Lidia, can significantly enhance vertical motion and upper-
799 level divergence conducive to RI. Operationally, diagnostic tools such as Trenberth forcing
800 and EFC metric could be integrated into forecasting to better assess trough-TC interactions.
801 Measuring these variables in real time would provide forecasters with actionable insights
802 into the likelihood of RI, particularly when TCs recurve toward the densely populated Pacific
803 coast of Mexico. Although the limitations of a single case study are evident, we suspect that
804 other RIs in the northeastern Pacific have been influenced by similar dynamical
805 mechanisms. However, while our results offer robust evidence from a synoptic-scale
806 perspective, this study is based on a single case. Future research should expand this
807 methodology to a broader set of events and explore complementary approaches using
808 convection-permitting high-resolution simulations. Such simulations would help resolve
809 inner-core processes and mesoscale interactions that were intentionally simplified in this
810 study, which focused on evaluating large-scale dynamical forcings. In this regard, the
811 framework proposed here serves as a cost-effective, scalable strategy to support RI
812 forecasting in regions with limited access to high-resolution modeling systems and highlights
813 the continued need to refine multi-scale diagnostic techniques for better understanding and
814 prediction of TC intensification. Also, expanding this methodology to a broader set of cases

815 could offer a more comprehensive understanding of trough-TC interactions and their role in
816 RI, ultimately improving operational forecasting capabilities in this understudied region.

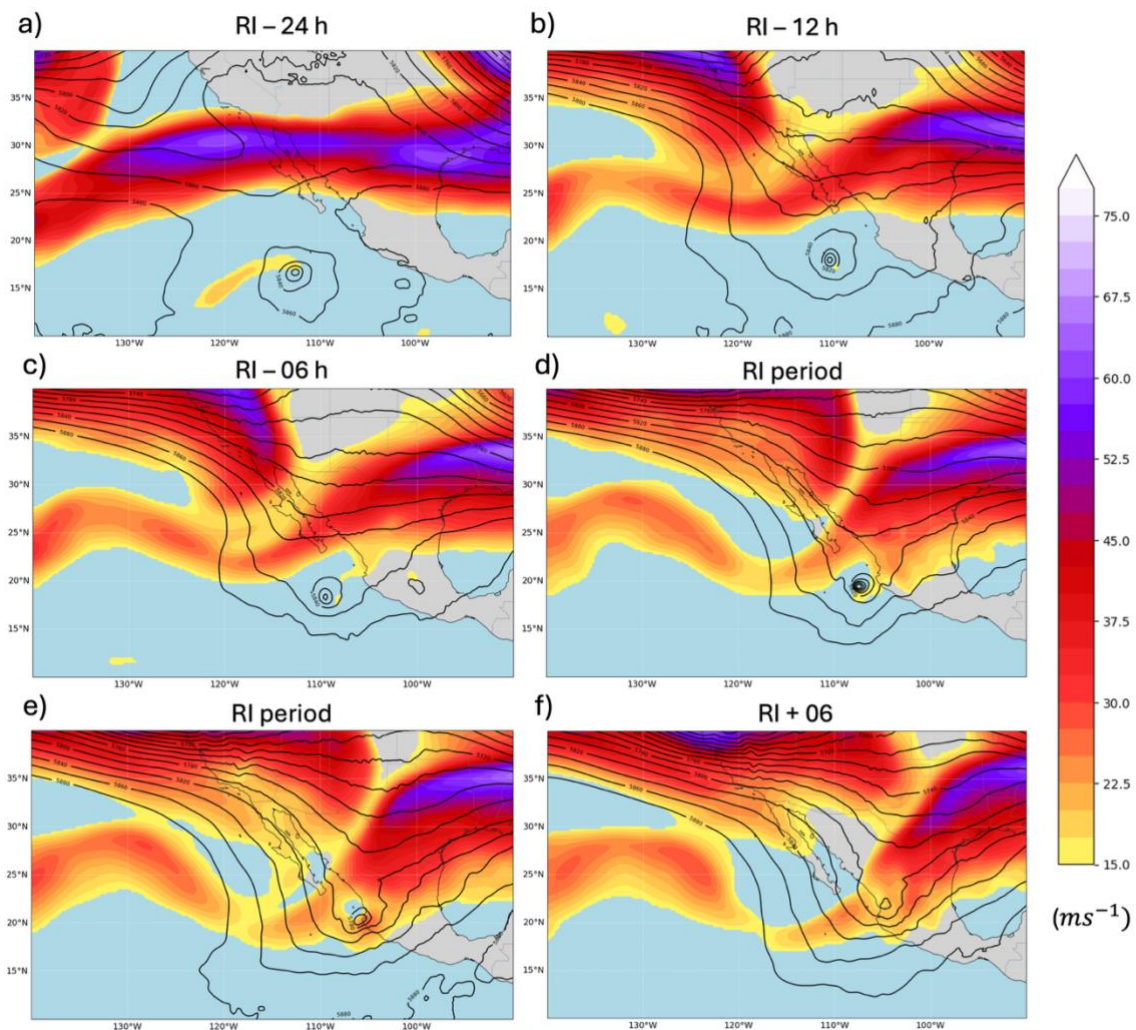
817

818 Appendix

819

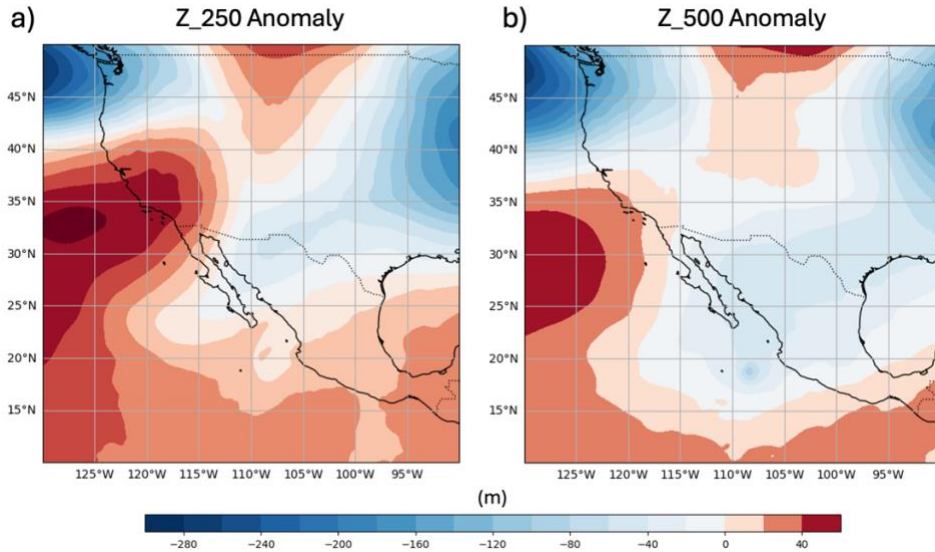
820 To complement and further clarify the dynamical interpretation presented in the main
821 manuscript, this Appendix provides three additional diagnostic figures that illustrate key
822 synoptic features relevant to Lidia's RI. Figure A1 documents the evolution of the upper-
823 tropospheric jet stream, offering temporal context for the intensifying trough-TC
824 interaction. Figure A2 shows geopotential height anomalies from ERA5, highlighting the
825 anomalous large-scale environment in which the RI occurred. Figure A3 presents the filtered
826 Trenberth forcing fields used to isolate the synoptic-scale contribution to vertical motion,
827 demonstrating that the main dynamical signals identified in the P_{80} -ensemble persist even
828 after suppressing the TC's inner-core circulation. Together, these supplementary diagnostics
829 reinforce the robustness of the mechanisms discussed in the main text and provide
830 additional transparency regarding the interpretation of the ensemble-based results.

831

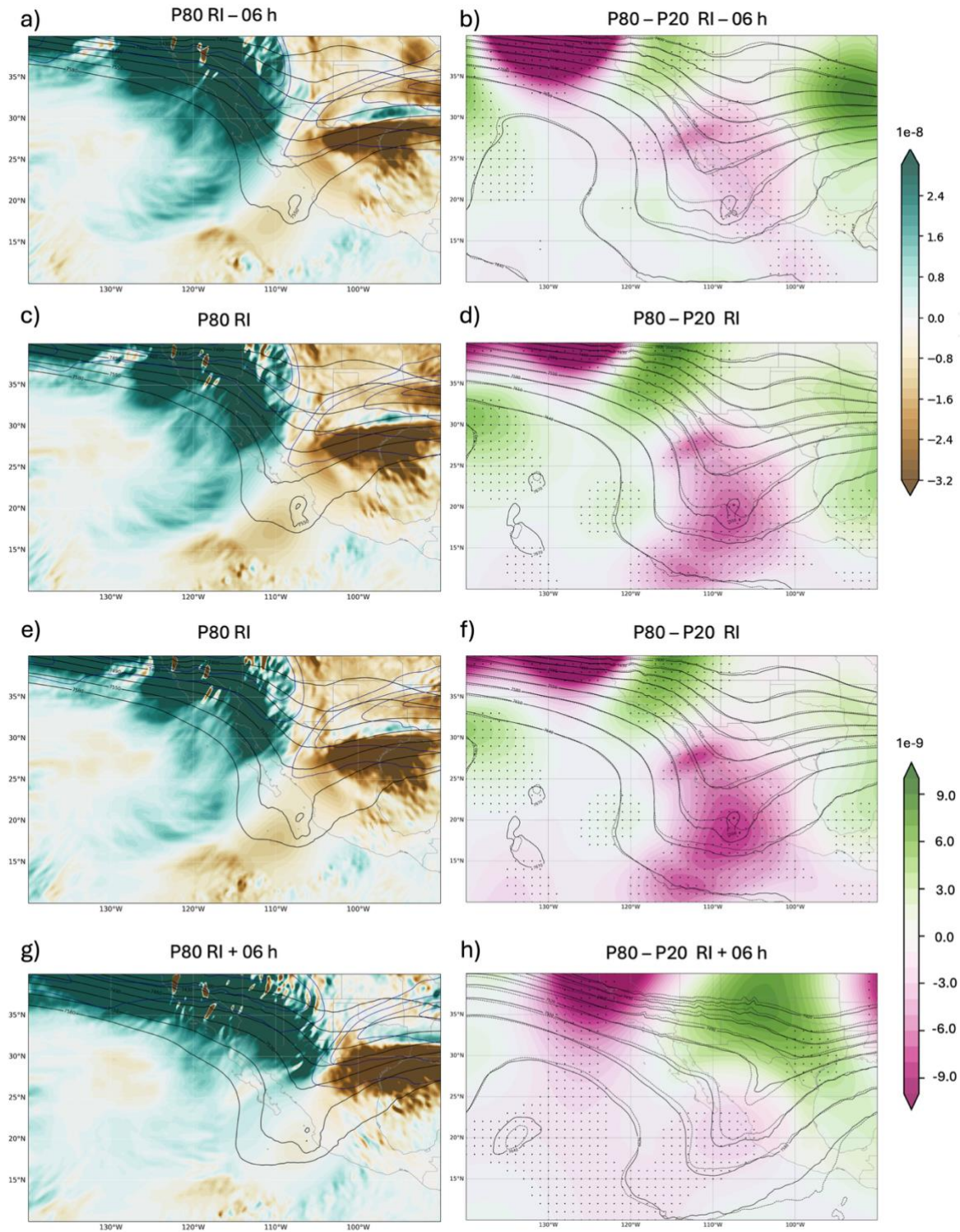


832

833 Figure A1. Upper-tropospheric jet stream before, during and after RI of Hurricane Lidia at
 834 250 hPa. Shaded colors denote wind speed (ms^{-1}), highlighting the jet stream core, while
 835 black contours represent geopotential height (gpm) at 500 hPa. Panels show consecutive
 836 time steps relative to the onset of RI: (a) -24 h, (b) -12 h, (c) -06 h, (d) onset RI period, (e)
 837 RI period, and (f) +06 h.
 838



839 Figure A2. Z anomalies from ERA5 for (a) 250 and (b) 500 hPa during the period surrounding
 840 Lidia's RI (12:00 UTC on 9 October, 2023). Warm (red) shading denotes positive height
 841 anomalies, while cool (blue) shading indicates negative anomalies.
 842



843
 844 Figure A3. (a, c, e, g) Filtered Trenberth forcing fields for the P_{80} -ensemble (left column) at
 845 selected times relative to the RI onset (-06 h, RI, $+06$ h). A Gaussian storm-centered filter (σ
 846 $= 2.5^\circ$ with a gradual taper of $\sigma = 1^\circ$) is applied to suppress the TC's inner-core circulation
 847 while retaining the synoptic-scale signal. Shading shows the filtered Trenberth forcing, and

848 black contours denote Z at 500-hPa. (b, d, f, h) Shading represents the $P_{80} - P_{20}$ of Trenberth
849 forcing, with contours showing the corresponding 500-hPa height fields from each
850 ensemble. Dots indicate grid points where the differences are statistically significant.

851

852 **Declaration of Competing Interest**

853

854 The authors declare no conflicts of interest relevant to this study.

855

856 **Acknowledgments**

857 This work was partially supported by the research project PID2023-146344OB-I00
858 (CONSCIENCE) financed by MICIU/AEI /10.13039/501100011033 and by FEDER, UE, and the
859 two ECMWF Special Projects (SPESMART and SPESVALE). Mauricio López-Reyes extends his
860 sincere gratitude to the Institute of IAM of the University of Guadalajara and Instituto
861 Frontera A.C., for his invaluable support. C. Calvo-Sancho acknowledges the grant awarded
862 by the Spanish Ministry of Science and Innovation - FPI program (PRE2020-092343), and
863 acknowledges support from the GVA. PROMETEO Grant CIPROM/2023/38; and CSIC-
864 LINCGLOBAL Ref. LINC24042. J.J. González-Alemán thanks support from the Spanish State
865 Meteorological Agency. Thanks to the two anonymous reviewers for their valuable
866 comments to improve this work and for the effort they made to review this manuscript.

867 **Open Research**

868

869 The tracking data for Hurricane Lidia can be found in López-Reyes, M. (2024). Atmospheric
870 data sets can be accessed through the MARS database, hosted by ECMWF, at
871 <https://confluence.ecmwf.int/display/MARS>. Additionally, ERA-5 reanalysis data base is
872 allowed in Climate Data Store (CDS; available at [https://climate.copernicus.eu/climate-](https://climate.copernicus.eu/climate-reanalysis)
873 reanalysis).

874

875 **Author contributions**

876

877 Conceptualization: MLR, MLMP, JJGA. Methodology: MLR, MLMP, CCS, JJGA. Project
878 administration: MLMP. Supervision: MLPM, CCS, JJGA. Writing-original draft: MLR. Writing-
879 review and edits: MLR, MLMP, CCS, JJGA.

880

881 **References**

882

883 Alland, J. J., Tang, B. H., Corbosiero, K. L., & Bryan, G. H. (2021). Combined Effects of Midlevel
884 Dry Air and Vertical Wind Shear on Tropical Cyclone Development. Part II: Radial Ventilation.
885 Journal of the Atmospheric Sciences, 78(3), 783-796. [https://doi.org/10.1175/JAS-D-20-](https://doi.org/10.1175/JAS-D-20-0055.1)
886 0055.1

887 Alland, J. J., Tang, B. H., Corbosiero, K. L., & Bryan, G. H. (2021). Combined Effects of Midlevel
888 Dry Air and Vertical Wind Shear on Tropical Cyclone Development. Part I: Downdraft

- 889 Ventilation. *Journal of the Atmospheric Sciences*, 78(3), 763-
890 782. <https://doi.org/10.1175/JAS-D-20-0054.1>
- 891 Avila, L. A., 1998: Forecasting tropical cyclone intensity changes: An operational
892 challenge. Preprints, *Symp. on Tropical Cyclone Intensity Change*, Phoenix, AZ, Amer.
893 Meteor. Soc., 1–3.
- 894 Billingsley, D. (1998). A review of QG theory—Part III: A different approach. *Natl. Wea.*
895 *Dig*, 22, 3-10.
- 896 Bister, M., & Emanuel, K. A. (2002). Low frequency variability of tropical cyclone potential
897 intensity 1. Interannual to interdecadal variability. *Journal of Geophysical Research:*
898 *Atmospheres*, 107(D24), ACL-26. <https://doi.org/10.1029/2001JD000776>
- 899 Bluestein, H. B. (1992). *Synoptic-dynamic Meteorology in Midlatitudes: Observations and*
900 *theory of weather systems* (Vol. 2). Taylor & Francis.
- 901 Bracken, W. E., & Bosart, L. F. (2000). The Role of Synoptic-Scale Flow during Tropical
902 Cyclogenesis over the North Atlantic Ocean. *Monthly Weather Review*, 128(2), 353-
903 376. [https://doi.org/10.1175/1520-0493\(2000\)128<0353:TROSSF>2.0.CO;2](https://doi.org/10.1175/1520-0493(2000)128<0353:TROSSF>2.0.CO;2)
- 904 Braun, S. A., & Tao, W.-K. (2000). Sensitivity of high-resolution simulations of Hurricane Bob
905 (1991) to planetary boundary layer parameterizations. *Monthly Weather Review*, 128(12),
906 3941–3961. [https://doi.org/10.1175/1520-0493\(2000\)129<3941:SOHRSO>2.0.CO;2](https://doi.org/10.1175/1520-0493(2000)129<3941:SOHRSO>2.0.CO;2)
- 907 Callaghan, J. (2020). WITHDRAWN: The interaction of Hurricane Michael with an upper
908 trough leading to intensification right up to landfall. *Tropical Cyclone Research and*
909 *Review*, 9(2), 135-142. <https://doi.org/10.1016/j.tccr.2019.07.009>
- 910 Cao, J., Ran, L., & Li, N. (2014). An Application of the Helmholtz Theorem in Extracting the
911 Externally Induced Deformation Field from the Total Wind Field in a Limited Domain.
912 *Monthly Weather Review*, 142(5), 2060-2066. <https://doi.org/10.1175/MWR-D-13-00311.1>
- 913 Carrasco, C., Landsea, C., & Lin, Y. (2014). The influence of tropical cyclone size on its
914 intensification. *Weather and Forecasting*, 29, 582–590. <https://doi.org/10.1175/WAF-D-13-00092.1>
- 916 Chen, H. & Gopalakrishnan, S. G. (2015). *A study on the asymmetric rapid intensification of*
917 *Hurricane Earl (2010) using the HWRF system. Journal of the Atmospheric Sciences*, 72(2),
918 531–550. <https://doi.org/10.1175/JAS-D-14-0097.1>
- 919 Chen, X., Zhang, J. A., & Marks, F. D. (2019). A thermodynamic pathway leading to rapid
920 intensification of tropical cyclones in shear. *Geophysical Research Letters*, 46(15), 9241-
921 9251. <https://doi.org/10.1029/2019GL083667>

- 922 Chen, Y., Gao, S., Li, X., & Shen, X. (2021). Key environmental factors for rapid intensification
 923 of the South China Sea tropical cyclones. *Frontiers in Earth Science*, *8*, 609727.
 924 <https://doi.org/10.3389/feart.2020.609727>
- 925 Chorin, A. J., Marsden, J. E., & Marsden, J. E. (1990). A mathematical introduction to fluid
 926 mechanics (Vol. 3, pp. 269-286). New York: Springer.
- 927 Collins, Clarence, Tyler Hesser, Peter Rogowski, and Sophia Merrifield. (2021). "Altimeter
 928 Observations of Tropical Cyclone-generated Sea States: Spatial Analysis and Operational
 929 Hindcast Evaluation" *Journal of Marine Science and Engineering* *9*, no. 2: 216.
 930 <https://doi.org/10.3390/jmse9020216>
- 931 DeMaria, M., Franklin, J. L., Onderlinde, M. J., & Kaplan, J. (2021). Operational forecasting
 932 of tropical cyclone rapid intensification at the National Hurricane Center. *Atmosphere*, *12*(6),
 933 683. <https://doi.org/10.3390/atmos12060683>
- 934 DeMaria, M., J. Kaplan, and J. Baik, 1993: Upper-Level Eddy Angular Momentum Fluxes and
 935 Tropical Cyclone Intensity Change. *J. Atmos. Sci.*, **50**, 1133–
 936 1147, [https://doi.org/10.1175/1520-0469\(1993\)050<1133:ULEAMF>2.0.CO;2](https://doi.org/10.1175/1520-0469(1993)050<1133:ULEAMF>2.0.CO;2).
- 937 DiMego, G. J., Bosart, L. F., & Endersen, G. W. (1976). An Examination of the Frequency and
 938 Mean Conditions Surrounding Frontal Incursions into the Gulf of Mexico and Caribbean
 939 Sea. *Monthly Weather Review*, *104*(6), 709-718. [https://doi.org/10.1175/1520-0493\(1976\)104<0709:AEOTFA>2.0.CO;2](https://doi.org/10.1175/1520-0493(1976)104<0709:AEOTFA>2.0.CO;2)
- 941 Dostalek, J. F., Schubert, W., DeMaria, M., Estep, D., Johnson, R., & Vonder Haar, T. (2012).
 942 Global omega equation: Derivation and application to tropical cyclogenesis in the North
 943 Atlantic Ocean.
- 944 Emanuel, K. A., & Lin, J. (2024, May). Hurricane Otis: A case for a rapid migration toward
 945 probabilistic tropical cyclone forecasting. Paper presented at the 36th Conference on
 946 Hurricanes and Tropical Meteorology, American Meteorological Society.
 947
- 948 Emanuel, K. A. (1986). An Air-Sea Interaction Theory for Tropical Cyclones. Part I: Steady-
 949 State Maintenance. *Journal of Atmospheric Sciences*, *43*(6), 585-
 950 605. [https://doi.org/10.1175/1520-0469\(1986\)043<0585:AASITF>2.0.CO;2](https://doi.org/10.1175/1520-0469(1986)043<0585:AASITF>2.0.CO;2)
 951
- 952 Emanuel, K. A. (1988). The maximum intensity of hurricanes. *J. Atmos. Sci.* *45*, 1143–1155.
 953 [doi:10.1175/1520-0469\(1988\)045<1143:tmioh>2.0.co;2](https://doi.org/10.1175/1520-0469(1988)045<1143:tmioh>2.0.co;2)
- 954 Fischer, M. S. (2018). Tropical cyclone rapid intensification in environments of upper-
 955 tropospheric troughs: Environmental influences and convective characteristics (Order No.
 956 10839442). Available from ProQuest One Academic. (2087658194). Retrieved from
 957 <http://wdg.biblio.udg.mx:2048/login?url=https://www.proquest.com/dissertations-theses/tropical-cyclone-rapid-intensification/docview/2087658194/se-2>
 958

959 Fischer, M. S., Tang, B. H., & Corbosiero, K. L. (2019). A Climatological Analysis of Tropical
960 Cyclone Rapid Intensification in Environments of Upper-Tropospheric Troughs. *Monthly*
961 *Weather Review*, 147(10), 3693-3719. <https://doi.org/10.1175/MWR-D-19-0013.1>

962 Fischer, M. S., Reasor, P. D., Tang, B. H., Corbosiero, K. L., Torn, R. D., & Chen, X. (2023). A
963 Tale of Two Vortex Evolutions: Using a High-Resolution Ensemble to Assess the Impacts of
964 Ventilation on a Tropical Cyclone Rapid Intensification Event. *Monthly Weather Review*,
965 151(1), 297-320. <https://doi.org/10.1175/MWR-D-22-0037.1>

966 García-Franco, J. L., Gómez-Ramos, O., & Domínguez, C. (2024). Hurricane Otis: the costliest
967 and strongest hurricane at landfall on record in Mexico. *Weather*, 79(6), 182-184.
968 <https://doi.org/10.1002/wea.4555>

969 Ge, X., Li, T., & Peng, M. (2013). Effects of Vertical Shears and Midlevel Dry Air on Tropical
970 Cyclone Developments. *Journal of the Atmospheric Sciences*, 70(12), 3859-3875.
971 <https://doi.org/10.1175/JAS-D-13-066.1>

972
973 Gilford, D. M. (2021). pyPI (v1. 3): Tropical cyclone potential intensity calculations in
974 Python. *Geoscientific Model Development*, 14(5), 2351-2369. <https://doi.org/10.5194/gmd-14-2351-2021>

975
976
977 Hanley, D., Molinari, J., & Keyser, D. (2001). A composite study of the interactions between
978 tropical cyclones and upper-tropospheric troughs. *Monthly weather review*, 129(10), 2570-
979 2584. [https://doi.org/10.1175/1520-0493\(2001\)129<2570:ACSOTI>2.0.CO;2](https://doi.org/10.1175/1520-0493(2001)129<2570:ACSOTI>2.0.CO;2)

980 Heming, J. T., Prates, F., Bender, M. A., Bowyer, R., Cangialosi, J., Caroff, P., ... & Xiao, Y. (2019).
981 Review of recent progress in tropical cyclone track forecasting and expression of
982 uncertainties. *Tropical Cyclone Research and Review*, 8(4), 181-218.
983 <https://doi.org/10.1016/j.tccr.2020.01.001>

984 Hersbach, H., Bell, B., Berrisford, P., Hirahara, S., Horányi, A., Muñoz-Sabater, J., ... &
985 Thépaut, J. N. (2020). The ERA5 global reanalysis. *Quarterly Journal of the Royal*
986 *Meteorological Society*, 146(730), 1999-2049. <https://doi.org/10.1002/qj.3803>

987 Hu, Yanyang, and Xiaolei Zou. (2021). "Tropical Cyclone Center Positioning Using Single
988 Channel Microwave Satellite Observations of Brightness Temperature" *Remote Sensing* 13,
989 no. 13: 2466. <https://doi.org/10.3390/rs13132466>

990 J.P. Cangialosi (2018). The State of Hurricane Forecasting. National Hurricane Center Blog–
991 Inside the Eye. [https://noaahc.wordpress.com/2018/03/09/the-state-of-](https://noaahc.wordpress.com/2018/03/09/the-state-of-hurricaneforecasting)
992 [hurricaneforecasting](https://noaahc.wordpress.com/2018/03/09/the-state-of-hurricaneforecasting)

993 Jin, R., Li, Y., Chen, X., & Li, M. (2023). Characteristics of the upper-level outflow and its
994 impact on the rapid intensification of Typhoon Roke (2011). *Frontiers in Earth Science*, 10,
995 1021308. <https://doi.org/10.3389/feart.2022.1021308>

- 996 Kaplan, J., & DeMaria, M. (2003). Large-scale characteristics of rapidly intensifying tropical
997 cyclones in the North Atlantic basin. *Weather and forecasting*, 18(6), 1093-1108.
998 [https://doi.org/10.1175/1520-0434\(2003\)018<1093:LCORIT>2.0.CO;2](https://doi.org/10.1175/1520-0434(2003)018<1093:LCORIT>2.0.CO;2)
- 999 Komaromi, W. A., & Doyle, J. D. (2018). On the dynamics of tropical cyclone and trough
1000 interactions. *Journal of the Atmospheric Sciences*, 75(8), 2687-2709.
1001 <https://doi.org/10.1175/JAS-D-17-0272.1>
- 1002 Larson, J., Zhou, Y., & Higgins, R. W. (2005). Characteristics of landfalling tropical cyclones in
1003 the United States and Mexico: Climatology and interannual variability. *Journal of*
1004 *Climate*, 18(8), 1247-1262. <https://doi.org/10.1175/JCLI3317.1>
- 1005 Leroux, M., Plu, M., & Roux, F. (2016). On the Sensitivity of Tropical Cyclone Intensification
1006 under Upper-Level Trough Forcing. *Monthly Weather Review*, 144(3), 1179-1202.
1007 <https://doi.org/10.1175/MWR-D-15-0224.1>
- 1008 Ling, S., Lu, R., & Cao, J. (2025). The variation in tropical cyclone genesis over the western
1009 North Pacific during the El Niño summers. *Climate Dynamics*, 63(1), 13.
1010 <https://doi.org/10.1007/s00382-024-07484-9>
- 1011 López-Reyes, M. (2024). Lidia's tracking. Zenodo.
1012 <https://doi.org/10.5281/zenodo.14187335>
- 1013 López Reyes, M., & Meulenert, A. (2021). Comparación de las variables físicas que influyen
1014 en la rápida intensificación de los ciclones tropicales del Océano Pacífico nororiental durante
1015 el periodo 1970-2018. *Cuadernos Geográficos*, 60(2), 105-125.
1016 <https://doi.org/10.30827/cuadgeo.v60i2.15474>
- 1017 López-Reyes, M., González-Alemán, J. J., Calvo-Sancho, C., Bolgiani, P., Sastre, M., & Martín,
1018 M. L. (2024). Remote Interactions between tropical cyclones: The case of Hurricane Michael
1019 and Leslie's high predictability uncertainty. *Atmospheric Research*, 107697.
1020 <https://doi.org/10.1016/j.atmosres.2024.107697>
- 1021 Liu, T., Liu, Z., Zhao, Y., & Zhang, S. (2024). Strong Extratropical Impact on Observed ENSO.
1022 *Journal of Climate*, 37(3), 943-962. <https://doi.org/10.1175/JCLI-D-23-0023.1>
- 1023 Loughe, A. F., Lai, C., & Keyser, D. (1995). A Technique for Diagnosing Three-Dimensional
1024 Ageostrophic Circulations in Baroclinic Disturbances on Limited-Area Domains. *Monthly*
1025 *Weather Review*, 123(5), 1476-1504. [https://doi.org/10.1175/1520-0493\(1995\)123<1476:ATFDTD>2.0.CO;2](https://doi.org/10.1175/1520-0493(1995)123<1476:ATFDTD>2.0.CO;2)
- 1027 Luna-Niño, R., Cavazos, T., Torres-Alavez, J. A., Giorgi, F., & Coppola, E. (2021). Interannual
1028 variability of the boreal winter subtropical jet stream and teleconnections over the CORDEX-
1029 CAM domain during 1980–2010. *Climate Dynamics*, 57(5), 1571-1594.
1030 <https://doi.org/10.1007/s00382-020-05509-7>

- 1031 Mann, H. B., & Whitney, D. R. (1947). On a Test of Whether one of Two Random Variables is
1032 Stochastically Larger than the Other. *The Annals of Mathematical Statistics*, 18(1), 50–60.
1033 <http://www.jstor.org/stable/2236101>
- 1034 Molinari, J., & Vollaro, D. (1990). External influences on hurricane intensity. Part II: Vertical
1035 structure and response of the hurricane vortex. *Journal of the Atmospheric sciences*, 47(15),
1036 1902-1918. [https://doi.org/10.1175/1520-0469\(1990\)047<1902:EIOHIP>2.0.CO;2](https://doi.org/10.1175/1520-0469(1990)047<1902:EIOHIP>2.0.CO;2)
- 1037 Montgomery, M. T., & Smith, R. K. (2025). Comments on “Marathon versus Sprint: Two
1038 Modes of Tropical Cyclone Rapid Intensification in a Global Convection-Permitting
1039 Simulation”. *Monthly Weather Review*, 153(2), 365-367. <https://doi.org/10.1175/MWR-D-24-0029.1>
- 1041 Richard J. Pasch (2024). Hurricane Milton Discussion Number 12 (Report). National
1042 Hurricane Center. Archived from the original on October 9, 2024. Retrieved October
1043 7, 2024.
- 1044 Richard J. Pasch (October 7, 2024). Tropical Cyclone Report: Hurricane Lidia (EP152023).
1045 National Hurricane Center. https://www.nhc.noaa.gov/data/tcr/EP152023_Lidia.pdf
- 1046 Riemer, M., & Montgomery, M. T. (2011). Simple kinematic models for the environmental
1047 interaction of tropical cyclones in vertical wind shear. *Atmospheric Chemistry and Physics*,
1048 11(17), 9395-9414. <https://doi.org/10.5194/acp-11-9395-2011>
- 1049 Peirano, C. M., Corbosiero, K. L., & Tang, B. H. (2016). Revisiting trough interactions and
1050 tropical cyclone intensity change. *Geophysical Research Letters*, 43(10), 5509-5515.
1051 <https://doi.org/10.1002/2016GL069040>
- 1052 Prasanth, S., Chavas, D. R., Marks Jr, F. D., Dubey, S., Shreevastava, A., & Krishnamurti, T. N.
1053 (2020). Characterizing the energetics of vortex-scale and sub-vortex-scale asymmetries
1054 during tropical cyclone rapid intensity changes. *Journal of the Atmospheric Sciences*, 77(1),
1055 315-336. <https://doi.org/10.1175/JAS-D-19-0067.1>
- 1056 RAMMB/CIRA Slider. (2024, October 1). GOES-16 visible satellite image. Retrieved from
1057 <https://rammb-slider.cira.colostate.edu/>
- 1058 Ríos-Berríos, R., Torn, R. D., & Davis, C. A. (2018). A closer look at the structure and intensity
1059 changes of rapidly intensifying tropical cyclones. *Monthly Weather Review*, 146(11), 3625–
1060 3645. <https://doi.org/10.1175/MWR-D-18-0111.1>
- 1061 Ryglicki, D. R., Velden, C. S., Reasor, P. D., Hodyss, D., & Doyle, J. D. (2021). Observations of
1062 Atypical Rapid Intensification Characteristics in Hurricane Dorian (2019). *Monthly Weather*
1063 *Review*, 149(7), 2131-2150. <https://doi.org/10.1175/MWR-D-20-0413.1>
- 1064 Ryglicki, D. R., Doyle, J. D., Hodyss, D., Cossuth, J. H., Jin, Y., Viner, K. C., & Schmidt, J. M.
1065 (2019). The Unexpected Rapid Intensification of Tropical Cyclones in Moderate Vertical Wind

- 1066 Shear. Part III: Outflow–Environment Interaction. *Monthly Weather Review*, 147(8), 2919-
1067 2940. <https://doi.org/10.1175/MWR-D-18-0370.1>
- 1068 Sadler J. (1975). *The upper tropospheric circulation over the global tropics*. University of
1069 Hawaii. Retrieved February 17, 2025, from
1070 <https://www.soest.hawaii.edu/Library/Sadler.html>
- 1071 Sato, K., Inoue, J., & Yamazaki, A. (2020). Performance of forecasts of hurricanes with and
1072 without upper-level troughs over the mid-latitudes. *Atmosphere*, 11(7), 702.
1073 <https://doi.org/10.3390/atmos11070702>
- 1074 Servicio Meteorológico Nacional. (2023, October 24). Special bulletin: Hurricane Otis rapid
1075 intensification and landfall warning [PDF]. Comisión Nacional del Agua (CONAGUA), Mexico.
1076 Retrieved from
1077 <https://smn.cna.gob.mx/tools/DATA/Ciclones%20Tropicales/Resumenes/2023.pdf>
- 1078 Sharma, N., & Varma, A. K. (2022). Impact of vertical wind shear in modulating tropical
1079 cyclones eye and rainfall structure. *Natural Hazards*, 112(3), 2083-2100.
1080 <https://doi.org/10.1007/s11069-022-05257-3>
- 1081 Shi, D., & Chen, G. (2021). The implication of outflow structure for the rapid intensification
1082 of tropical cyclones under vertical wind shear. *Monthly Weather Review*, 149(12), 4107-
1083 4127. <https://doi.org/10.1175/MWR-D-21-0141.1>
- 1084 Shi, D., & Chen, G. (2023). Modulation of Asymmetric Inner-Core Convection on Midlevel
1085 Ventilation Leading up to the Rapid Intensification of Typhoon Lekima (2019). *Journal of*
1086 *Geophysical Research: Atmospheres*, 128(7), e2022JD037952.
1087 <https://doi.org/10.1029/2022JD037952>
- 1088 Smith, R. K., Kilroy, G., & Montgomery, M. T. (2021). Tropical cyclone life cycle in a three-
1089 dimensional numerical simulation. *Quarterly Journal of the Royal Meteorological Society*,
1090 147(739), 3373-3393. <https://doi.org/10.1002/qj.4133>
- 1091 Stevenson, S. N., Corbosiero, K. L., & Molinari, J. (2014). The Convective Evolution and Rapid
1092 Intensification of Hurricane Earl (2010). *Monthly Weather Review*, 142(11), 4364-4380.
1093 <https://doi.org/10.1175/MWR-D-14-00078.1>
- 1094 Tan, Z. M., Lei, L., Wang, Y., Xu, Y., & Zhang, Y. (2022). Typhoon track, intensity, and structure:
1095 From theory to prediction. *Adv. Atmos. Sci.* 39, 1789–1799 [https://doi.org/10.1007/s00376-](https://doi.org/10.1007/s00376-022-2212-1)
1096 [022-2212-1](https://doi.org/10.1007/s00376-022-2212-1)
- 1097 Tang, B., & Emanuel, K. (2010). Midlevel Ventilation’s Constraint on Tropical Cyclone
1098 Intensity. *Journal of the Atmospheric Sciences*, 67(6), 1817-1830.
1099 <https://doi.org/10.1175/2010JAS3318.1>

- 1100 Tang, B., & Emanuel, K. (2012). A Ventilation Index for Tropical Cyclones. *Bulletin of the*
 1101 *American Meteorological Society*, 93(12), 1901-1912. [https://doi.org/10.1175/BAMS-D-11-](https://doi.org/10.1175/BAMS-D-11-00165.1)
 1102 00165.1
- 1103 Tao, D., Van Leeuwen, P. J., Bell, M., & Ying, Y. (2022). Dynamics and predictability of tropical
 1104 cyclone rapid intensification in ensemble simulations of Hurricane Patricia (2015). *Journal*
 1105 *of Geophysical Research: Atmospheres*, 127(8), e2021JD036079.
 1106 doi.org/10.1029/2021JD036079
- 1107 Tong, B., Wang, X., Wang, D., & Zhou, W. (2023). A Novel Mechanism for Extreme El Niño
 1108 Events: Interactions between Tropical Cyclones in the Western North Pacific and Sea Surface
 1109 Warming in the Eastern Tropical Pacific. *Journal of Climate*, 36(8), 2585-2601.
 1110 <https://doi.org/10.1175/JCLI-D-21-1014.1>
- 1111 Wang, Y., Li, Y., Xu, J., Tan, Z. M., & Lin, Y. (2021). The intensity dependence of tropical cyclone
 1112 intensification rate in a simplified energetically based dynamical system model. *Journal of*
 1113 *the Atmospheric Sciences*, 78(7), 2033-2045. <https://doi.org/10.1175/JAS-D-20-0393.1>.
- 1114 Winters, A. C., & Attard, H. E. (2022). North Pacific and North Atlantic Jet Covariability and
 1115 Its Relationship to Cool Season Temperature and Precipitation Extremes. *Weather and*
 1116 *Forecasting*, 37(9), 1581-1600. <https://doi.org/10.1175/WAF-D-21-0203.1>
 1117
- 1118 Wu, L., Su, H., Fovell, R. G., Dunkerton, T. J., Wang, Z., & Kahn, B. H. (2015). Impact of
 1119 environmental moisture on tropical cyclone intensification. *Atmospheric Chemistry and*
 1120 *Physics*, 15(24), 14041-14053. <https://doi.org/10.5194/acp-15-14041-2015>
 1121
- 1122 Zhang, D. L., & Chen, H. (2012). Importance of the upper-level warm core in the rapid
 1123 intensification of a tropical cyclone. *Geophysical Research Letters*, 39(2).
 1124 <https://doi.org/10.1029/2011GL050578>
 1125
- 1126 Zhang, J. A., Rogers, R. F., Reasor, P. D., Uhlhorn, E. W., & Marks, F. D., Jr. (2013). Asymmetric
 1127 Hurricane Boundary Layer Structure from Dropsonde Composites in Relation to the
 1128 Environmental Vertical Wind Shear. *Monthly Weather Review*, 141(11), 3968-
 1129 3984. <https://doi.org/10.1175/MWR-D-12-00335.1>
 1130
- 1131 Zhang, F., & Emanuel, K. (2016). On the Role of Surface Fluxes and WISHE in Tropical Cyclone
 1132 Intensification. *Journal of the Atmospheric Sciences*, 73(5), 2011-
 1133 2019. <https://doi.org/10.1175/JAS-D-16-0011>
 1134
- 1135 Zhao, Haikun, & Raga, Graciela B.. (2015). On the distinct interannual variability of tropical
 1136 cyclone activity over the eastern North Pacific. *Atmósfera*, 28(3), 161-178. Recuperado en
 1137 14 de noviembre de 2025, de: <https://doi.org/10.20937/ATM.2015.28.03.02>